

SC5076.2TR  
AD A034487

12  
SC5076.2TR

COPY NO. 6

IMPACT DAMAGE IN CARBON/CARBON COMPOSITES

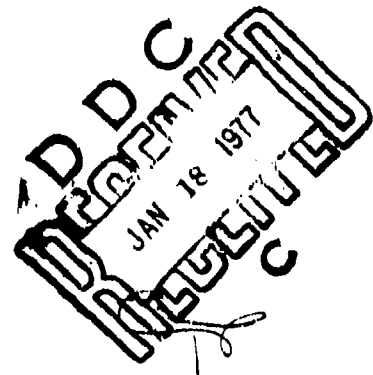
Technical Report

May 1, 1976 thru Dec. 31, 1976

Contract No. N00014-76-C-0854

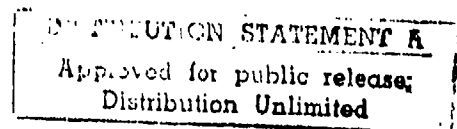
Submitted to:

Office of Naval Research  
800 N. Quincy Street  
Arlington, VA 22217



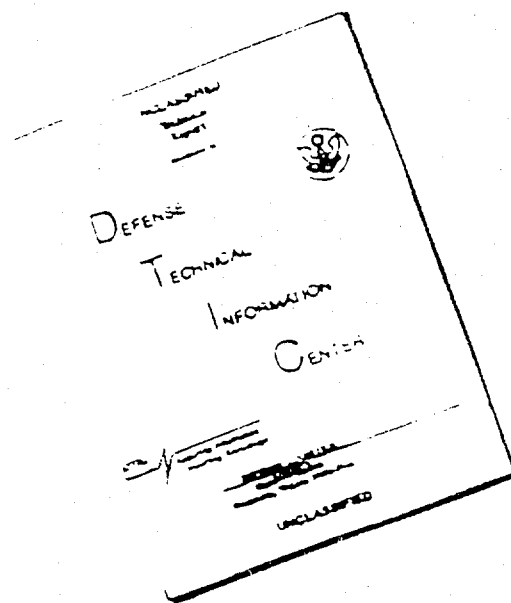
Reproduction in Whole or in Part is Permitted for  
any purpose of the United States Government

This Research was Sponsored by the Office of Naval Research  
Under Contract No. N00014-76-C-0854 (Project No. 471)



Science Center  
Rockwell International

# DISCLAIMER NOTICE



THIS DOCUMENT IS BEST QUALITY AVAILABLE. THE COPY FURNISHED TO DTIC CONTAINED A SIGNIFICANT NUMBER OF PAGES WHICH DO NOT REPRODUCE LEGIBLY.

Unclassified

SECURITY CLASSIFICATION OF THIS PAGE (When Data Entered)

REPORT DOCUMENTATION PAGE		READ INSTRUCTIONS BEFORE COMPLETING FORM
1. REPORT NUMBER	2. GOVT ACCESSION NO.	3. RECIPIENT'S CATALOG NUMBER
4. TITLE (and Subtitle) IMPACT DAMAGE IN CARBON/CARBON COMPOSITES.		5. TYPE OF REPORT & PERIOD COVERED Technical May 1, 1976 thru Dec. 31, 1976
7. AUTHOR(s) A. G./Evans, W. F./Adler and J. C./Chesnutt		6. PERFORMING ORG. REPORT NUMBER SC5076.2TR
9. PERFORMING ORGANIZATION NAME AND ADDRESS Rockwell International, Science Center, Thousand Oaks, CA 91360		8. CONTRACT OR GRANT NUMBER(s) N00014-76-C-0854
11. CONTROLLING OFFICE NAME AND ADDRESS Office of Naval Research 800 N. Quincy Street Arlington, VA 22217		10. PROGRAM ELEMENT, PROJECT, TASK AREA & WORK UNIT NUMBERS Project No. 471 (NR032-570)
14. MONITORING AGENCY NAME & ADDRESS (if different from Controlling Office) <i>(12) [88 p.]</i>		12. REPORT DATE 31 Dec 1976
		13. NUMBER OF PAGES 85
		15. SECURITY CLASS. (of this report) Unclassified
		15a. DECLASSIFICATION/DOWNGRADING SCHEDULE
16. DISTRIBUTION STATEMENT (of this Report) Approved for Public Release; distribution unlimited		
<i>(1) Technical rept. 1 May - 31 Dec 76.</i>		
17. DISTRIBUTION STATEMENT (of the abstract entered in Block 20, if different from Report)		
18. SUPPLEMENTARY NOTES		
19. KEY WORDS (Continue on reverse side if necessary and identify by block number) Carbon composites, impact, erosion, damage modes, fracture, kinking		
20. ABSTRACT (Cont. us on reverse side if necessary and identify by block number) The damage to carbon-carbon composites created by projectile impacts has been characterized for a range of test conditions and for several weave constructions and processing variables. A number of subsurface damage modes have been identified (on sectioned specimens) in the vicinity of the crater produced by particulate impingement. In addition, studies are underway to determine the modes of failure which occurred in the material ejected from the crater. Preliminary analyses of the primary subsurface damage modes have been undertaken to define the approach that would elucidate the microstructural dependence of the impact		

Unclassified

SECURITY CLASSIFICATION OF THIS PAGE(When Data Entered)

damage.



Unclassified

SECURITY CLASSIFICATION OF THIS PAGE(When Data Entered)

SC5076.2TR

IMPACT DAMAGE IN CARBON/CARBON COMPOSITES

Interim Technical Report  
for the period 05/01/76 thru 12/31/76

GENERAL ORDER NO. 5076

CONTRACT NO. N00014-76-C-0854

Project No. 471 (NR032-570)

Prepared for:

Office of Naval Research  
800 North Quincy Street  
Arlington, VA 22217

by

A. G. Evans\*, W. F. Adler<sup>‡</sup> and J. C. Chesnutt\*

\*Science Center, Rockwell International, Thousand Oaks,  
CA 91360

<sup>‡</sup>Effects Technology, Inc., 5383 Hollister Ave.,  
Santa Barbara, CA 93111



North American Rockwell  
Science Center

1049 CAMINO DOS RIOS  
THOUSAND OAKS, CALIF 91320  
805/498 4343

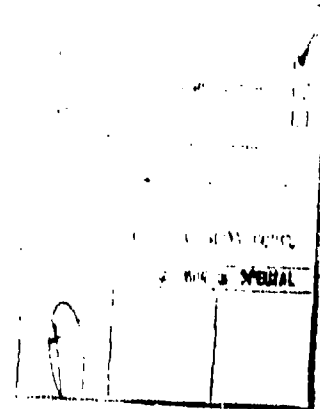


TABLE OF CONTENTS

	<u>Pg.</u>
1.0 INTRODUCTION	1
2.0 IMPACT DAMAGE OBSERVATIONS	4
2.1 Overview of Crater Formation	4
2.2 Investigative Procedure	9
2.3 Observations	10
2.2.1 Damage Perspectives	10
2.2.2 Damage Details	11
a) Low Temperature	11
b) Elevated Temperatures	13
3.0 QUASI-STATIC STUDIES	14
3.1 Indentation Tests	14
3.2 Penetration Tests	14
3.3 Compliance Tests	15
3.4 Micromechanics Tests	16
4.0 DAMAGE ANALYSIS	18
4.1 Preliminary Assessment	18
4.2 Detailed Analysis	18
4.2.1 Kinking	19
4.2.2 Longitudinal Fiber Fracture	23
4.2.3 Lateral Fiber Fracture	25
5.0 CONCLUSION	26
APPENDIX I	27
APPENDIX II	29
REFERENCES	31
FIGURE CAPTIONS	34

ABSTRACT

The damage to carbon-carbon composites created by projectile impacts has been characterized for a range of test conditions and for several weave constructions and processing variables. A number of subsurface damage modes have been identified (on sectioned specimens) in the vicinity of the crater produced by particulate impingement. In addition, studies are underway to determine the modes of failure which occurred in the material ejected from the crater. Preliminary analyses of the primary subsurface damage modes have been undertaken to define the approach that would elucidate the microstructural dependence of the impact damage.

## 1.0 INTRODUCTION

Investigation of the erosive response of fibrous composites exposed to natural (rain/ice) and induced (dust) particulate environments is stimulated by the need for re-entry vehicle protection materials. The erosion performance of existing system materials have been evaluated using ground impact simulation testing and verification flight tests.<sup>1-6</sup> In the evaluation of materials fabricated for improved erosion resistance, all material evaluation has been directly related to erosion test performance. Little attention has been given to information for material development activities. Traditionally, material suppliers fabricated materials for erosion test evaluation and found the test data provided only limited insight as to why a given material performed either well or poorly. It has been difficult for material manufacturers to relate erosion test results such as mass loss ratios to material construction or processing variables.

Historically, efforts directed toward determination of mass loss due to particulate impact of re-entry vehicle materials have been largely experimental and primarily of two types: single particle impact testing<sup>6</sup> and continuous erosion testing in ballistic range facilities.<sup>1-3</sup> Mass loss laws were derived for specific materials based on correlations of the results from these types of experiments. In the case where single particle data were used, the possible effects of multiple particle collisions were not represented. In the case where continuous erosion data were used, the laws focused on the result and not the process of erosion. In both cases extrapolation to service conditions was made from a limited data base and without consideration of the physical process by which cratering occurs. Recently, the process of mass removal in single particle impacts on virgin material has been placed on a more solid physical basis<sup>7</sup>; however, even this analysis is incomplete.

It has been recently found that each single particle impact causes substantial damage in addition to mass loss.<sup>8-9</sup> Furthermore, it has been found that after many sequential single particle impacts on one specimen the average mass loss for each test is considerably higher than the base line single particle value. It has been postulated that this increase in average mass loss is due to subsurface interaction of damaged material. This increase is now referred to as "damage enhancement" in light of its postulated cause.

Damage enhancement is possibly the most sensitive parameter in erosion mass loss. Experimental values of up to 3.3 have been recorded. It is also a complex function of extrinsic variables such as velocity, particle size, particle type and temperature as well as intrinsic variables such as material properties and material failure modes. The present work is directed toward quantifying the extent and nature of the subsurface damage produced by a variety of impact conditions and to assess the contribution of the most significant aspects of the subsurface damage to damage enhancement. The ultimate objective of this study will be to suggest microstructural modifications, in terms which are meaningful to a material fabricator, that would improve the erosion resistance of carbon composites.

A number of other programs have been carried out in the general areas considered in this report. This previous work has been reviewed and will be utilized in achieving the objectives of the current program; however, there are several factors which differentiate the work underway. For example, the post-test examinations of the impacted specimens are being correlated with information gained from high-speed photographic studies and other experimental procedures, in order to construct the details of the cratering process, from initial contact to damage completion.

The present study has, thus far, consisted of an examination of the damage in a number of carbon-carbon systems (Table I)\* created by glass, Nylon and water projectiles, over a wide range of temperature (0 - 3600°C), and velocity (1800-5500 ms<sup>-1</sup>), as required to identify the primary modes of failure. Quasistatic experiments which provide some of the ancillary information required to analyze the observed failure modes have been designed and implemented. Finally, preliminary analysis of certain damage modes has been initiated.

---

\* The specimens for investigation within this program were obtained from a concurrent and broader based SAMSO program, F04701-76-C-0069, and an Air Force program, Contract No. F33615-75-C-5214.

## 2.0 IMPACT DAMAGE OBSERVATIONS

### 2.1 Overview of Crater Formation

The conditions mainly used for the damage analysis are single particle tests produced by 1 mm glass beads, using the impact facility described in Appendix A. High speed photographic sequences have been taken of a limited number of particle impacts.\* Both ATJ-S graphite and GE223 carbon-carbon were investigated in this way.

For ATJ-S graphite at low impact velocities (a 1 mm glass bead impacting at 300 m/s) the collision produces an annular fracture zone surrounding what appears to be a pedestal of compressed material (Figure 1a). In some cases a portion of the material in the annular fracture zone remains in place (displaying a petaled appearance) but is nearly completely separated from the bulk material. At slightly higher velocities the central pedestal begins to be removed and the configuration of the cross section changes, as shown in Fig. 1b. A relatively smooth annular region can be identified in most cases (to be referred to as surface spallation) surrounding the deeper fracture annulus. The high speed photographic sequence in Fig. 2 shows the development of an outward conical spray of material from the surface and a schematic representation of how this configuration may come about is shown in Fig. 3.

At the same time the outflow of material is taking place the material surrounding the impacting sphere is rapidly compressed as seen in Fig. 4. At

---

\* Carried out under SAMSO Contract F04701-76-C-0069.

these velocities a shock wave propagates away from the contact zone in both the target and the glass bead. Due to the spherical shape of the glass bead the shock pulse will attenuate and reflected waves will be propagated from the free surface. The cumulative wave interactions will produce significant tensile stresses in the glass bead which eventually produce tensile normal stresses at the interface and the mutual contact terminates. The tensile stresses in the glass sphere become more intense as the impact velocity increases: eventually fracturing and fragmentation of the sphere takes place. Fragmentation of the sphere can occur as it is propelled away from the impact zone, however, a velocity regime is finally achieved for which the glass bead fragments in a time which is less than twice the transient time of the shock pulse across the diameter of the sphere. A large portion of the fragmented glass is then confined to the interior of the crater.

The penetration of the glass sphere into ATJ-S graphite is governed in part by rapid compression of the target material below the sphere. When the applied constraint of the impacting sphere is removed due to fragmentation or rebound, the highly compressed material attempts to regain its initial state. This process occurs partly due to the rapidity of the compression phase and the non-equilibrium nature of the material's response, and partly because of plasticity effects (matrix densification and, at high temperatures, fiber deformation - see section 3) which allows tensile waves to be developed by reflection at the elastic/plastic interface. The immediate elastic response of the compressed material causes it to be projected outward from the crater. The former effect is vividly demonstrated for the case of a tungsten carbide sphere impacting at 1.2 km/s. The 1 mm diameter sphere is found embedded in the interior of the target material, however the path it followed in the penetration process is completely resealed with disturbed material, as illustrated in Fig. 5.

The high speed photographs show an outpouring of material along the perpendicular to the surface of the target as depicted in Fig. 6. This phase of crater formation becomes more important as the velocity increases; but, even at relatively low impact velocities (e.g.,  $2000 \text{ ms}^{-1}$  for a 1 mm glass sphere impacting ATJ-S), it continues for more than an order of magnitude longer than the particle spray phase described earlier. Tensile stresses sufficient to produce cohesive failures in the target exist at depths well below the penetration depth; however, not all of the material affected by the impact becomes ejected before the material in the vicinity of the impact zone can relax to its new equilibrium state. Fractured but non-ejected material is seen below the crater on microradiographs of X-ray opaque impregnated sections of ATJ-S graphite.

As already stated a shock wave is propagated into the target in concert with the penetration process. The shock spreads outward from the damage zone when the penetration velocity falls below the shock speed. The relaxation of the material surrounding the crater should certainly be related to the passage of this shock wave; but, another aspect of shock formation and propagation is the influence of the free surface. Shock reflections at the free surface can produce rarefaction waves near the surface of the target resulting in spallation of an annular region around the mouth of the crater; however, the details of this process are not yet fully understood.

The relative timing of the sequence of events described here should be kept in mind. At high impact velocities the particle spray phase occurs quite rapidly in relation to the overall cratering process, corresponding approximately to the velocity of an attenuating shock wave moving outward from the contact zone. The roughened surface of the contact zone will be enveloped by the sphere and carried downward during the sphere penetration stage. The presence of this roughened zone on the contact interface could produce minor perturbations in the early target/

sphere interfacial pressure distribution. The sphere continues to deform as it penetrates, so the particle velocity and pressure at the actual target/sphere interface are fairly complex functions of the depth of penetration. A rarefaction wave will be reflected into the substrate due to the presence of a free surface as the shock wave moves outward. The crater itself also introduces a second free surface and the stress distributions in the region surrounding the lip of the crater involve complex interactions between the reflected stress waves. The exact manner in which relaxation of the material near the surface and adjacent to the crater wall takes place is not clear, but it should be noted that material removal along the crater wall probably initiates before the region below the impacting sphere shows extensive relaxation. The vertical thrust of the material from beneath the crater carries fragments freed from the sidewalls out of the crater: the crater expands both in depth and lateral extent.

The shock related damage comprises only the very earliest stages of the penetration process. The penetration velocity of the sphere rapidly decelerates but a highly fractured sphere (in the case of glass beads) or a deforming sphere (in the case of Nylon beads) continues to embed itself in the target material. This process imposes a direct pressure on the material surrounding the particle which produces damage in addition to the shock-related damage. The role of the inertia of the expanding cavity boundary may also impose a direct pressure on the underlying material, even after the glass sphere disintegrates. These effects will be described in Section 2.3.

A similar sequence of events to that described for ATJ-S graphite takes place during the impact process in 223 carbon-carbon specimens, however the general damage modes in the material are strongly influenced by the three-dimensional fiber network. High-speed photographic sequences of 1 mm glass and Nylon beads impacting 223 carbon-carbon specimens at  $2440 \text{ ms}^{-1}$  are shown in Fig. 7. The initial conical spray (shown at a higher framing rate in Fig. 8)

develops followed by ejection of material perpendicular to the face of the specimen as a central plume rising out of the crater. Referring to Fig. 7, it is seen in a frame by frame comparison for the two types of beads that the velocity with which the central plume leaves the crater is somewhat less for the Nylon bead impact than that due to the glass bead. Measurements of these velocities and that for another impact are provided in Fig. 9. The glass particle can be seen leaving the crater in Fig. 7(a). An additional observation which can be made from these photographs is that the diameter of the base of the plume approaches a diameter of approximately 1 mm.

The high-speed photographic studies are useful in trying to establish some perspective on the loading sequence, and dominant failure modes which have occurred in the material removed from the crater. The velocities of various features of the crater formation sequence are indicated in Fig. 10. It is seen by tracing the temporal changes in the location of a distinctive feature in the plume that the approximate time at which it was freed from the crater can be reconstructed. Although the photographic sequence extends over hundreds of microseconds the cratering process itself was probably completed within 20  $\mu$ s. Measurements can also be made of the expansion of the spray diameter from Fig. 8, as indicated in Fig. 11. The maximum diameter is quickly established.

The surface spallation observed for ATJ-S graphite takes on a very preferential nature for 223 carbon-carbon as shown in Fig. 12 and is now manifested as a stripping of the surface fibers. The longitudinal wave speeds in the fibers are higher than those for the laminated series of transverse fibers and matrix material. In 223 the set of lateral fibers exposed on the surface will be subjected to this stripping action. The specimens shown in Fig. 12 were specially prepared. The specimen in Fig. 12(a) was metallographically polished and the specimen in Fig. 12(b) was thoroughly impregnated with epoxy and then metallographically

polished. These same surface features occur in normally prepared specimens but the fiber stripping is less uniform. By filling the voids and general defects in the composite's microstructure with epoxy an excellent pattern is achieved showing the extent of the damage due to surface shock interactions. Both of these surfaces were photographed prior to impact. In both cases the extent of the damage appears to be quite localized and no fine-scale damage was observed beyond the area encompassed by the fiber stripping boundary.

## 2.2 Investigative Procedure

Scanning electron microscope (SEM) plan views of the craters provide a general comparison of the nature of the damage observed from one test condition to another and for the various carbon-carbon systems currently represented in the test program. The crater is scanned for details of the surface fracture modes. Subsequently, the specimens are sectioned. The method used is to mount the specimen in epoxy to preserve the details of the microstructure during subsequent sectioning operations. It was found that by using an outgassing procedure, the epoxy resin completely permeates the interior of the specimen. The prepared specimen is then sectioned either along a plane near the periphery of the crater or along the mid-plane of the crater. The sectioning is carried out using a wire saw at the lowest possible cutting rate. The section is then metallographically polished. The microscopic observations of progressive cross sections are being used to establish a three-dimensional picture of the extent and nature of the subsurface damage and its relation to the SEM observations of the damage within the crater.

Some specimens have not been impregnated with epoxy. These samples were used to observe the character of the damage within severely fractured zones in the vicinity of the crater, wherein material removal had occurred upon sectioning.

## 2.3 Observations

### 2.2.1 Damage Perspectives

A sequence demonstrating the development of the impact damage at low temperatures (0 - 2500°C), as a function of projectile velocity (for 1 mm glass projectiles), is presented in Figs. 13,14. At velocities below  $\sim 2000 \text{ ms}^{-1}$  the projectile is retained by the target (Figs. 13,a,b,d,e) and the crater consists primarily of a central zone that accommodates the penetration of the projectile (Figs. 13,d,e). However, at higher velocities (Figs. 13c,14a,b) the projectile is ejected, and the crater contains an outer ledge in addition to a more deeply penetrating central zone. Also, as already noted, surface stripping of the lateral bundles (Fig. 14a) is an additional damage mode that becomes manifest at the higher velocities. Close inspection of the central zone (Fig. 15) indicates the existence of accommodation damage; this clearly suggests that the central zone is related to the penetration of the projectile (as at the lower velocities). An initial evaluation of the effect of microstructure (see Table I) on the damage morphology (Fig. 16) indicates that the central penetration zone tends to increase in depth, while the outer ledge diminishes in width, as the proportion of longitudinal fibers increases. Kinking of certain lateral fiber bundles near the crater periphery is also apparent in certain microstructures (Fig. 17a), and the presence of short lengths of longitudinal fibers laterally displaced away from the impact center (Figs. 17b) is commonly observed on longitudinal bundles in the crater ledge.

The damage created by deformable projectiles (water or Nylon) has most of the same features (Fig. 18), although there is little evidence of accommodation damage in the central zone. Under multiple impact conditions (Fig. 18c), linking of the outer ledge damage zones occurs at closely spaced impacts.

At high temperatures ( $\approx 3000^\circ\text{C}$ ) the impact damage is again quite similar

(Fig. 19), except that the impact is accompanied by permanent distortion of the fibers adjacent to the central zone, (Fig. 19b) and by the creation of permanent interfibre separations (Fig. 19c).

### 2.2.2 Damage Details

#### a) Low Temperature ( $\approx 3000^\circ\text{C}$ )

The detailed nature of the impact damage created at high velocity ( $\approx 2500 \text{ ms}^{-1}$ ) has been obtained on sections. The principal modes of damage identified in this study are summarized in schematic overviews (Figs. 20,21,22). Sections close to the center of impact that contain the longitudinal fiber bundles (Fig. 20) show that the longitudinal bundles directly beneath the central penetration zone (2 fibers for a 1 mm projectile) are extensively kinked and that the lateral bundles over a larger area are permanently displaced in the vertical direction. The kinking of the longitudinal bundles occurs in both the in-plane and out-of-plane modes (Fig. 23). The in-plane kinks (Fig. 23) result from in-plane buckling and are characterized by the fibers lying within the plane of view. The kinks are inclined to the bundle axes at angles  $\phi_k$  ranging from  $\sim 40$  to  $50^\circ$  (both positive and negative), and the kink boundaries invariably bisect the obtuse angle at the kinks ( $180 - \phi_k$ ). The out-of-plane kinks derive from out-of-plane buckles and are identified by fiber ends being in evidence within the plane of view (Fig. 23), and the kink boundaries are on planes orthogonal to the fiber axis. These kink morphologies are schematically summarized in Fig. 24. No clear relation between the kink mode within the longitudinal bundles and the location of the adjacent lateral bundles could be discerned. The kinks are narrow, and generally extend across the entire bundle, except at kink intersections (Fig. 9c,d,f) or pre-existing defects (Fig. 23) where kink arrest occurs. Microfracture invariably occurs at the kink boundaries (Fig. 23) and some macrofracture of the longitudinal fibers is apparent near the crater boundary (Fig. 9a,b).

The adjacent sections (Fig. 21) show that several layers of lateral bundles exhibit kinking which extends well beyond the periphery of the crater. These kinks are all in-plane (Fig. 25) and generally even narrower than the kinks in the longitudinal bundles. There is also a distinct fiber orientation relation (see Fig. 24); positive near the crater, mixed at a distance  $\sim 7d$  from the center of impact (where  $d$  is the bundle thickness) and then predominantly negative at larger distances. This kinking often initiates at sites close to the corner of an out-of-plane lateral fiber bundle. Additional kinking and distortion of the lateral bundles is apparent under the impact center, especially where orthogonal lateral bundles juxtapose (Fig. 26). Inspection of these fiber failures indicates mixed mode kinking, usually on a plane between the opposite corners of the adjacent out-of-plane lateral bundles (Fig. 26b,e). However, some tensile fractures (Fig. 26c) and simple kinking (Fig. 20c) can also be detected. Directly beneath the crater (Fig. 26a,d) the failure is complex and the damage seems to be more intense in a region adjacent to the matrix zone.

Near the crater periphery, the damage is quite different (Fig. 22). There is no apparent kinking, but two modes of fracture occur. Firstly, the lateral fibers fracture on planes near the surface (Fig. 27). Secondly, the longitudinal fibers fracture (Fig. 28) almost invariably at sites adjacent to an in-plane lateral bundle/matrix interface. The fractures are apparent on planes adjacent to (Fig. 28a) and below (Fig. 28b) the crater surface.

The damage created at low velocities ( $\approx 2500 \text{ ms}^{-1}$ ) has many of the same characteristics as the high velocity damage, except that the kinking is less extensive and different in character. Specifically, the kinking of the lateral fibers is confined to a small zone around the impact center (Fig. 29a) and usually, these kinks do not extend across the entire bundle (Fig. 29b).

Similarly the kinking of the longitudinal fibers (Fig. 29c) is localized to a zone directly beneath the position of maximum penetration, and the kinks are complex and broad.

b) Elevated Temperatures ( $\approx 3000^{\circ}\text{C}$ )

The impact damage at elevated temperatures can again be essentially characterized by the features summarized in Figs. 20, 21 and 22, but the damage details exhibit important differences from those discerned at low temperatures. Extensive permanent fiber distortion occurs at the crater surface (Fig. 30) which indicates that the fibers are capable of limited plastic extensions prior to fracture. The kinking is less extensive (Fig. 31), especially along the lateral fibers (Figs. 30,32), and fiber fracture does not invariably occur at the kink boundary (Fig. 32); rather, the kink strain is accommodated in a significant proportion of fibers by a permanent distortion mechanism. Also, the kinks usually arrest before they propagate through the fiber bundles. The plastic strain prior to fracture is not large enough at the temperatures employed in the present study ( $\approx 3600^{\circ}\text{C}$ ) to prevent a significant proportion of fractures occurring at the kink boundaries. The kinking is still, therefore, a mode of material degradation up to  $\sim 3600^{\circ}\text{C}$ ; although a transition to fully plastic kinking could occur at even higher temperatures.

The characteristics of the other primary damage modes, complex kinking, distortion and fracture of the lateral fibers beneath the impact center (Fig. 33) and fiber fracture in the outer ledge, do not differ significantly from the characteristics observed at low temperatures.

### 3.0 QUASI-STATIC STUDIES

#### 3.1 Indentation Tests

Indentation tests have been performed using 2 mm diameter tungsten carbide spheres. The damage observed (Fig. 24) is quite similar to that obtained at low impact velocities ( $\approx 2000 \text{ ms}^{-1}$ ). Kinking and fracture of the longitudinal fibers occurs (Fig. 34a); however, the number of kinks is smaller than observed under impact conditions, and the kinks are broader. An intensely deformed layer was apparent at the crater surface (Fig. 34b); this layer was presumably ejected in the impact experiments. This layer could be easily removed by immersion in an ultrasonic cleaner to reveal a crater (Fig. 34c) similar to the central zone of the impact craters. Uplift and surface stripping of the lateral fibers was also in evidence.

#### 3.2 Penetration Tests

An instrumented drop tower was used for penetration tests. This test is considered dynamic in a sense that it involves penetration velocities of a few meters per second, (which is four orders of magnitude greater than conventional static loading rates). These tests typically last a few milliseconds, which is convenient for high temperature measurements. By directly instrumenting the penetrator, reasonably accurate measurements of the load and deflection could be obtained simultaneously. A deflection gauge system was used for penetration measurements. Two Biomation Model 802 Transient Records are used to record load and deflection signals. The records were synchronized by a Tetrax FG 501 Function Generator. The information was digitized, fed into a Hewlett-Packard Model 9830A computer, and stored on magnetic tape. The raw data could then be plotted or further processed. The final result is a plot of penetration pressure,  $p$ , versus depth of penetration (normalized to the indenter diameter)  $q/D$ . A curve fitting

procedure of the form<sup>13</sup>

$$p = p_0 (q/D)^n \quad (1)$$

is then applied to the data. The coefficient  $p_0$  is the pressure at one diameter of penetration, while the exponent  $n$  is the slope of the pressure/penetration curve. The parameters  $p_0$  and  $n$  are determined by a least mean square fit. An example of this analysis is shown in Fig. 35 for a penetration test on GE223 material at 1000°C. Penetration pressures,  $p_0$ , have been obtained on GE223 carbon-carbon at temperatures up to 3500°C, and compared with the temperature dependence of the mass loss (Fig. 36). Tests have also been performed on several different materials in the virgin and obscured surface state. Again these results have been compared with mass loss measurements (Fig. 37). Opposite trends in the correlation between mass loss and dynamic penetration pressure are apparent in the two test sequences. However, it is premature to infer from these results that the dynamic penetration pressure is not one of the parameters which determines the extent of the impact damage, because several aspects of the present penetration tests (e.g. the scale of the penetration zone) suggest that penetration conditions equivalent to those that prevail in the mass loss tests have not yet been achieved.

### 3.3 Compliance Tests

The compliance of each zone of the composite was evaluated using a micro-compressive test (Fig. 38). This test consisted of a determination of the force ( $P$ ), displacement ( $y$ ) behavior of individual zones, using a 400  $\mu\text{m}$  diameter tungsten carbide hemisphere. The approximate Young's modulus,  $E$ , of each zone was then determined from the relation,<sup>14</sup>

$$E = \frac{P}{y} \frac{(1-\nu^2)}{2a_r} \quad (2)$$

where  $a_r$  is the radius of the hemisphere, and  $\nu$  is Poisson's ratio.

The force, deflection behavior, summarized in Fig. 38, indicates that the longitudinal fibres exhibit the maximum stiffness  $E$  ( $\approx 30$  GPa),<sup>‡</sup> while the

<sup>‡</sup> The greater stiffness of fiber composites in the longitudinal direction is a well-documented effect; the ratio of the lateral to longitudinal stiffness depends on the fiber loading, the matrix material, etc.<sup>15</sup>

lateral fibers (in both locations) and the matrix have a similar stiffness ( $E \approx 5 \text{ GPa}$ ) at low stress levels ( $\approx 80 \text{ MPa}$ ). However, the matrix becomes non-linear at stresses  $\approx 80 \text{ MPa}$  (due to a permanent compression associated with the porosity), and thereafter the effective tangent modulus decreases continuously with strain.

### 3.4 Micromechanics Tests

For complex problems, such as the present impact damage problem, a possible approach for evaluating the effects of microstructure on the primary damage modes is to perform simulated micromechanics tests that allow each damage mode to be studied independently, under well defined boundary conditions. Such an approach has been initiated herein by separating fiber bundles from the composite (to retain the exact state of impregnation experienced within the composite), and then setting individual bundles, or arrays of bundles, into specified matrices. The bundle separation has been achieved using a  $75 \mu\text{m}$  thickness dicing saw with a microscopic aligning system. Initially, individual bundles have been set into epoxy matrices and buckling, under conditions of uniform compression, has been examined. Critical buckling stresses  $\sigma_b$  were obtained by direct optical observation. The relation between the buckling stress and the matrix modulus obtained for a range of matrices is plotted in Fig. 39.

The buckling of a beam on an elastic foundation, modulus  $\beta$ , under uniform compression usually occurs at a stress given by;<sup>16</sup>

$$\sigma_b = \frac{\pi^2}{12} E_b \left( \frac{d}{\lambda} \right)^2 + \frac{\beta}{\pi^2} \left( \frac{\lambda}{d} \right)^2 \quad (3)$$

where  $d$  is the dimension of the beam cross section,  $\lambda$  is the beam length, and  $E_b$  is the beam modulus. Hence, eqn (3) indicates that the critical buckling stress should vary linearly with the foundation modulus; also the slope should relate

to the effective cross section ( $d^2$ ) for beam buckling, while the zero modulus intercept should exhibit an additional dependence on the effective modulus of the beam. The anticipated linear relation is consistent with the test data (Fig. 39), and the slope suggests an effective buckling cross section equal to the total cross section of the bundle. The bundle can, therefore, be considered to buckle, at least to a very good approximation, as a single entity. The effective modulus of this entity derived from the intercept of Fig. 39 is 50 GPa. This is in the same range as the approximate value deduced from the localized compliance measurements (section 3.3). Studies are now in progress to determine the effect on buckling of bundle/bundle interactions and non-uniform compressive stress distributions.

## 4.0 DAMAGE ANALYSIS

### 4.1 Preliminary Assessment

A preliminary analysis of the present impact damage observations and quasi-static micromechanics tests indicates that several modes of failure are occurring during impact and that each of these should be treated as a separate but inter-related entity. The key aspects of the damage process are as follows:

i) Damage can derive from both the compressive stresses (kinking) and the tensile stresses (fracture) generated by the impact. The more expansive damage (kinking) results from the compressive stresses; this is in contrast to most brittle materials<sup>17</sup> which are subject to intensive (lateral and radial) fracture that derives primarily from the tensile stresses.

ii) The crater configurations obtained using glass projectiles suggest that the central zone develops due to the direct penetration of the projectile, in a manner analogous to the deep penetration of metals.<sup>13</sup> However, the details of the penetration are, of course, quite different in the case of carbon fiber composites, consisting primarily of fiber kinking and pore collapse, with some plasticity.

iii) There is an outer ledge to the crater which appears to develop by a different sequence of events than the central penetration zone. Firstly, the radially oriented lateral fibers fail by kinking, primarily due to the compressive stresses. However, the absence of kinking in both the longitudinal fibers and the tangentially oriented lateral fibers suggests that these fibers fail (presumably at a subsequent stage) due to a combination of shear and tensile stresses.

### 4.2 Detailed Analysis

Detailed analysis of the primary failure modes (observed in the present study) has been initiated, in order to identify the microstructure that provides

the optimum overall resistance to impact damage. The study is not yet complete, but some progress has been achieved in the analysis of each failure mode. The status of these analyses is discussed in the following sections.

#### 4.2.1 Kinking

Kinking occurs when a buckling instability develops.<sup>18</sup> This generates tensile bending stresses in the fiber which exceed the fiber fracture stress at various (statistically distributed) locations along the fiber (Fig. 40). The micromechanics tests have indicated (Section 3.3) that an evaluation of the kinking phenomena in carbon composites might be performed by regarding the bundles as single entities. Further, since the small strain compliance of the lateral fiber bundles and matrix are essentially the same (Section 3), the foundation modulus for small lateral end deflections of the bundles can be considered constant and the buckling problem for the longitudinal bundles can be treated as buckling on an elastic homogeneous foundation. This is consistent with the observations (Fig. 23) that there are no clear relations between the kinking mode and the lateral bundle locations. However, the end deflections for the lateral bundles are larger and an analysis of lateral buckling might require that the orthogonal lateral bundles be regarded as positions of higher stiffness. This might account for the significant proportion of kinks that initiate adjacent to the corners of orthogonal lateral fiber bundles (Fig. 25).

##### 4.2.1.1 Critical Buckling (Kinking) Stresses

The compressive stresses generated by projectile impact are time and position dependent, such that the spatial extent of the compressive zone increases with time (i.e. as the shock front expands), while the peak stress,  $\sigma_m$ , decreases with time. The buckling of beams in the presence of such variable compressive forces is predicated on the spatial extent of the compressive field ( $\lambda_p$ ), the peak compressive stress ( $\sigma_m$ ), and the detailed spatial variation

of the stress. The latter only affects the numerical values of the proportionalities in the buckling relations, and dimensional relations between the buckling variables can be specified without knowing these details. For an isolated beam<sup>16</sup>

$$\sigma_{mc} = C_1 \left( \frac{d_b}{\lambda_b} \right)^3 \left[ 1 + C_2 \frac{\beta}{E_b} \left( \frac{\lambda_b}{d_b} \right)^4 \right] \quad (4)$$

where  $\sigma_{mc}$  is the critical value of the peak stress needed to cause buckling,  $\beta$  is the foundation modulus,  $C_1$  and  $C_2$  are the constants that depend on the detailed stress distribution and  $d_b$  is the bundle diameter. The buckling length in the present impact problem would thus be approximately equal to the distance between the shock front and the impact site.

Therefore, it can be deduced that several material parameters exert an important influence on the kinking depth. (i) The elastic/plastic properties of the material are important because they determine the stress/time/position characteristics for the impact and thus dictate both the locations at which buckles occur (via eqn 4) and the shape of the buckles. (ii) The flaw sizes and distributions in the fibers are important because they determine the location(s) in the buckle that become the preferred sites for kinking. (iii) The bundle diameter is important since it decreases the tendency for buckling for a specified stress history (eqn 4); however, this benefit could be counteracted if the bundle diameter affects the impact stresses by modifying the elastic and plastic properties in the impact direction (cf. section 2). (iv) the bundle separation may also influence the kinking by enhancing the effective foundation modulus that pertains to the fiber beneath the impact center; but, again the present observations (section 2) indicate that this may be more than offset by the effect of the concomitant change in the elastic and plastic properties in the impact direction.

The elucidation of kink resistant microstructures thus requires that further experiments and analysis be performed which enable the separate effects of microstructure on the impact stresses and the buckling and kinking tendencies to be deduced. The effects of temperature on the extent of kinking can, however, be qualitatively appreciated in terms of the reduced dynamic stresses that derive from the lower impact pressures and elastic moduli.

#### 4.2.1.2 Kink Morphologies

The orientations of the kinks and the location of the kink boundaries are dictated by the strain energy and surface energy changes that derive from the kinking process, and can be predicted in a manner analogous to Griffith's treatment of crack propagation.<sup>19</sup> A simplified form of this analysis, which yields quite accurate predictions of the kink orientation parameters, considers only the strain energy changes caused by kinking.\*

Firstly, examine the kink initiation process (Fig. 41b). The initial fiber fracture essentially establishes the kink orientation and thus, determines the strain energy due to kinking that resides in the matrix; at this stage, the strain energy changes that occur in the fiber bundle are relatively small. To illustrate the analysis a preliminary two-dimensional approximation for the kink orientation  $\phi$  is derived by evaluating the orientation which yields the maximum release of shear strain energy within the matrix. The matrix shear strain energy,  $U_b$ , in the initial buckled state, for a sinusoidal buckle in a through-thickness fiber (or laminate) of unit thickness is (Appendix II)

$$U_b = \mu m (\pi \epsilon_1 \delta_0)^2 / x_0 \quad (5)$$

---

\* This simplified analysis neglects surface energy changes; this is a reasonable approximation for the kinking process; but is quite unacceptable, of course, for the analogous crack propagation problem.

The strain energy per unit thickness in the kinked state,  $U_k$ , which derives from the shear strain in the matrix adjacent to the kink is given (Appendix II) by;

$$U_k \approx \epsilon_2^2 (\Delta d) \mu_m \tan \phi / 2 \quad (6)$$

The strain energy change during initial kinking is thus

$$\Delta U = U_b - U_R = \mu_m \left[ \frac{(\pi \epsilon_1 \delta_0)^2}{x_0} - \epsilon_2^2 (\Delta d) \tan \phi_k \right] \quad (7)$$

Differentiating eqn (7) with respect to  $\phi$  gives

$$\frac{\partial \Delta U}{\partial \phi} = -\epsilon_2^2 (\Delta d) \frac{(\cos^2 \phi - \sin^2 \phi)}{\cos^2 \phi} \quad (8)$$

then equating to zero to determine the kink inclination  $\phi_k$  that yields the maximum strain energy release shows that,  $\phi_k = 45^\circ$ . This result compares very favorably with the observed kink inclinations (see Section 2).

The kink propagation path (the kink boundary) is determined primarily by the strain energy release associated with fiber fracture. Consider the extension of a kink by the fracture of a fiber at the kink 'tip'. Strain energy release occurs in both halves of the fractured fiber (Fig. 41), and the total strain energy change  $\Delta U_f$  per unit thickness is simply (Appendix II);

$$\Delta U_f = -d_f \mu_f (\tan^2 \theta_1 + \tan^2 \theta_2) / 2 \quad (9)$$

Specifying a constant kink orientation  $\phi_k$  (equal to the sum,  $\theta_1 + \theta_2$ ), differentiating eqn (9) with respect to  $\theta_1$ , and setting the differential to zero to obtain the maximum, gives

$$\theta_1 = \theta_2 = \phi_k / 2 \quad (10)$$

The kink boundary should thus bisect the included kink angle, a result that is entirely consistent with the observed fiber morphology at the kink interface (Section 2 ).

#### 4.2.2 Longitudinal Fibre Fracture

In the outer ledge, the location of fracture of the longitudinal bundles at the lateral bundle/matrix interface (Fig. 28a) and the planar character of the fracture (Fig. 16) strongly suggest that these failures derive primarily from localized shear stresses. These shear stresses could arise after the initial shock wave has degenerated into an elastic/plastic wave. (The presence of a substantial tensile component would lead to uncorrelated fiber failures at statistically distributed planes of weakness, as observed in many composite systems.) The observed failure might thus be envisaged as a shear dominated fracture along the matrix / lateral bundle interface with the longitudinal bundles as the restraining ligaments (Fig. 42). A preliminary estimate of the parameters involved in this failure process can be obtained by evaluating the shear failure of individual ligaments.

The displacements and stresses in the ligament can be deduced by noting that the ligament deformation (Fig. 42) is equivalent to that of two opposing rigidly mounted cantilevers in intimate contact. The cantilever solution<sup>14</sup> indicates that the lateral displacement,  $v$ , (Fig. 42) is;

$$v = \frac{P \delta^3}{E_b d_b^4} \quad (11)$$

where  $E_b$  is the bundle modulus,  $d_b$  is the bundle diameter and  $\delta$  is the width of the shear zone;  $P$  is the load applied to the cantilever, which is related to the average shear stress,  $\tau_R$ , by

$$P = \tau_R (d_b + d_s)^2 \quad (12)$$

where  $d_s$  is the separation between adjacent ligaments.

The peak tensile stress,  $\sigma_m$ , occurs at two locations (A or A' in Fig. 42). However, the fracture process would dominate at one of these locations, leaving a partial fracture at the other location. This process may account for the short fiber segments observed on the fractured longitudinal fibers in the outer ledge (Fig. 17b). The magnitude of the peak tensile stress is given by:<sup>14</sup>

$$\sigma_m = \frac{6 P \delta}{d_b^3} \quad (13)$$

Equating  $\sigma_m$  to the effective tensile strength of the fibers,  $\sigma_{eff}$ , the critical shear resistance of the ligaments,  $\tau_{Rc}$ , and the corresponding critical displacement,  $v_c$ , can be obtained (by combining eqns (11) (12) and (13)) as;

$$\tau_{Rc} = \frac{\sigma_{eff} d_b^3}{6 \delta (d_b + d_s)^2} \quad (14a)$$

$$v_c = \frac{\delta^2 \sigma_{eff}}{6 E_b d_b} \quad (14b)$$

where  $\sigma_{eff}$  is the difference between the actual fiber fracture stress,  $\sigma_f$ , and the tensile stress,  $\sigma_a$ , at the shearing ligament. If it is assumed that the fracture is a stress controlled process, eqn (14a) would predict that the longitudinal fiber fracture should be more difficult and hence, that the extent of the outer ledge be diminished, as the fracture stress of the fibers and the bundle diameter increase or as the bundle separation decreases. Such a trend has been observed in the present studies (Section 2, Fig. 16), adding further credence to the suggestion that a shear dominated bundle failure occurs in this zone.

#### 4.2.3 Lateral Fiber Fracture

The lateral fiber fractures (Fig. 27) are generally less correlated than the longitudinal fiber fractures, and appear to be more typical of the fractures expected from a substantial tensile component of stress. The fractures appear to derive from the bending associated with the approximate spherical symmetry of the dynamic stress stress field. These bending stresses could be augmented by localized bending around longitudinal fibers, especially where relatively large displacements occur which allow permanent matrix compressions to initiate. A possible relation for lateral fiber fracture might thus require that the local radius of curvature,  $R$ , be equal to a critical value,  $R_c$ , given by;

$$R_c = \frac{E_b d_b}{2\sigma_f} \quad (15)$$

## 5.0 CONCLUSION

The damage created in carbon composites by the impact of projectiles has been characterized. The damage has compressive failure characteristics (kinking) and tensile fracture characteristics (fracture) in various constituents of the microstructure; in addition, localized zones of permanent deformation have been observed, especially at elevated temperatures.

The sequence in which the damage is created in various zones of the damaged region has been discussed, and elementary models that identify the important microstructural parameters involved in the damage process have been derived. Micromechanics tests that allow some quantification of these damage mechanisms have also been initiated.

APPENDIX IParticle Impact Test Facility

The erosion test facility consists of a high energy capacitor discharge exploding foil system and associated diagnostic equipment. Laboratory test methods have been developed for launching single and multiple particles at hypersonic velocities with a high degree of reliability, for controlling the impact site with great accuracy, for observing the condition of the particle in flight just prior to impact, and for accurately measuring the impact velocity.

The launching method is based upon established exploding foil technology. With foil connected across the capacitor bank, the charging switch is closed, and the capacitor bank is charged to the desired voltage. The series circuit is completed by ionizing the air in the spark gap. Air ionization is initiated by applying a high voltage pulse to a pair of pointed electrodes located between the capacitor electrodes. The pulse is obtained from a high voltage trigger generator and coupled to the trigger electrodes through a step-up transformer. Breakdown of the spark gap initiates discharge of the capacitor bank through the foil, and the resulting high amplitude current flowing through the foil causes the foil to explode. The foil is part of a carefully fabricated assembly.

For complete characterization of the erosion resistance of materials, the testing facility has the capability to perform impact testing up to 3600°C. A commercial induction heating unit has been installed which is capable of heating a 0.5 inch diameter by 0.5 inch long specimen to 3600°C in two to three seconds. In the high temperature range, the temperature of the specimen is determined using an automatic optical pyrometer with temperature range of 1800 to 3600°C.

Diagnostics systems which are used in the particle impact test facility include active systems for dynamic measurements performed during the test (e.g., particle velocity, impact time, particle integrity) and passive systems for determining test parameters and results (e.g., particle mass, particle diameter, mass loss, crater dimensions).

APPENDIX IISHEAR STRAIN ENERGIES OF BUCKLED AND KINKED FIBER BUNDLES1. Sinusoidal Buckle

The shear strain,  $\gamma_b$ , in a matrix element,  $dx$ , adjacent to a sinusoidal buckle of unit thickness is;

$$\gamma_b = \frac{\pi \delta_0}{x_0} \cos \left( \frac{\pi x}{x_0} \right) \quad (A1)$$

where  $\delta_0$  is the peak amplitude of the buckle, and  $x_0$  is its wavelength. The elastic strain energy,  $dU_b$ , in a volume element  $dx$  of unit width is thus;

$$dU_b = \frac{\mu_m (\xi_1 \gamma_b)^2}{2} dx = \frac{\mu_m}{2} \left( \frac{\pi \xi_1 \delta_0}{x_0} \right)^2 \cos^2 \left( \frac{\pi x}{x_0} \right) dx \quad (A2)$$

where  $\mu_m$  is the shear modulus of the matrix, and  $\xi_1$  is a constant that relates  $\gamma$  to its average value over unit width and thereby allows for a decrease in  $\gamma$  with distance from the matrix/fiber interface. The total shear strain energy in a buckle of one wavelength (assuming that  $\xi_1$  is independent of  $x$ ) is thus;

$$U_b = \int_0^{x_0} dU_b \approx \frac{\mu_m}{x_0} (\pi \xi_1 \delta_0)^2 \quad (A3)$$

2. Kinked Fiber2.1 Matrix Strain Energy

The strain,  $\gamma_m$ , in the matrix adjacent to a kink oriented at an angle  $\phi$  with respect to the fiber axis (Fig. 41) is simply;

$$\gamma_m = \tan \phi \quad (A4)$$

If, for simplicity, the matrix strain is assumed\* to be located in a matrix element equal in width to the kink width,  $l_k$ , the strain energy in the matrix per unit thickness is

$$U_k \approx \frac{\mu_m}{2} (\epsilon_2 \gamma_m)^2 l_k \equiv \frac{\mu_m}{2} \Delta d \epsilon_2^2 \tan \phi \quad (A5)$$

where  $\epsilon_2$  is a constant (similar to  $\epsilon_1$ ) that allows  $\gamma$  to decrease with distance from the matrix/kink interface, and  $\Delta d$  is the kink displacement (Fig. 41) that, for a single kink, would be  $\approx \delta_0$ .

## 2.2 Fiber Strain Energy

The strain  $\gamma_f$  in each half of a kinked, but intact, fiber (Fig. 42) in the vicinity of the kink is;

$$\gamma_f = \tan \theta_{1,2} \quad (A6)$$

The strain energy,  $U_f$ , per unit thickness in each fiber half is thus

$$U_f = \frac{\mu_f}{2} d_f \tan^2 \theta_{1,2} \quad (A7)$$

where  $\mu_f$  is the shear modulus of the fiber and  $d_f$  is the fiber diameter.

## ACKNOWLEDGEMENT

The authors are indebted to M. Metcalf, P. Sauers and E. Wright for their extensive and expert experimental assistance in this work.

---

\* The dependence of  $U_k$  on  $\phi$ , which is the important dependence for the present analysis of kink orientations (Section 4), is the same for this simplified case as that obtained for more realistic spatial dependencies of the matrix strain.

REFERENCES

1. R. J. Sullivan and R. R. Hockridge, Simulation Techniques for Hypersonic Erosion Phenomena, Proc. Fourth Int. Conf. on Rain Erosion and Associated Phenomena, Mursburg, West Germany (May 1974).
2. R. B. Mortensen, Advanced Erosion Test Facilities, Proc. Fourth Int. Conf. on Rain Erosion and Associated Phenomena, Mursburg, West Germany (May 1974).
3. W. G. Reinecke, Rain Erosion at High Speeds, Proc. Fourth Int. Conf. on Rain Erosion and Associated Phenomena, Mursburg, West Germany (May 1974).
4. J. D. Carlyle, M. E. Graham, and T. L. Menna, Development of the Particle Impact Test Facility, Effects Technology, Inc. Presented at the 25th Meeting of the Aeroballistic Range Association, Naval Ordnance Laboratory, October 1974.
5. J. D. Carlyle, M. E. Graham, and T. L. Menna, Particle Impact Calibration Test Results, Effects Technology, Inc. Presented at the 25th Meeting of the Aeroballistic Range Association, Naval Ordnance Laboratory, October 1974.
6. J. D. Carlyle, M. E. Graham, and T. L. Menna, Facility for High Speed Particle Impact Testing, Review of Scientific Instruments, vol. 46, No. 9, pages 1221-1225, September 1975.
7. ETI Erosion Modeling Program, SAMSO Contract F04701-76-C-0069.
8. K. Kratsch, et al., Exploratory Development and Investigation of Carbon-Carbon Composite Materials Having Improved Hypersonic Particle Erosion Resistance - CHIP (Carbon Hypersonic Impact Program), AFML-TR-75-157 (Sept., 1975).
9. L. Rubin, Impact Damage Mechanisms of 3-D Carbon-Carbon Material, SAMSO TR-76-142 (July 1976).

10. E. M. Ross, The Carbon-Carbon Assessment Program, AFML-TR-74-39 (September 1974).
11. R. J. Miller, Mechanics of Erosion - Phase I, DNA 3446F-1 (November 1974).
12. J. H. Oscarson and R. J. Sullivan, Mechanics of R/V Rain and Dust Erosion, DNA 3614F (August 1975).
13. J. N. Goodier, 'Proceedings of Seventh Hypervelocity Impact Symposium' 3 215 (1965).
14. S. Timoshenko and J. N. Goodier, Theory of Elasticity (McGraw Hill, New York) 1951.
15. T. Dimmock and M. Abraham, Composites, December 1969, p. 87.
16. S. Timoshenko and J. M. Gere, Theory of Elastic Stability, (McGraw Hill, N.Y.) 1961.
17. A. G. Evans, M. E. Gulden, G. E. Eggum, and M. Rosenblatt, 'Impact Damage in Brittle Materials in the Plastic Response Regime,' Science Center Report SC5023.9TR (October 1976).
18. C. W. Weaver and J. G. Williams, Jnl. Mater. Sci. 10, 1323 (1975).
19. A. A. Griffith, Phil. Trans. Roy. Soc. 221A, 163 (1920)

TABLE 1. GENERAL CHARACTERISTICS OF SPECIMENS UNDER INVESTIGATION

MATERIAL DESIGNATION	REINFORCING FIBERS	PROCESSING	NUMBER OF ENDS			UNIT CELL DIMENSIONS* (mils)			BULK DENSITY** (g/cc)
			X	Y	Z	X	Y	Z	
GE223	T50	CVD + pitch	2	2	3	33	33	30	1.87
418	BM-1000/3000 (PAN)		2	2	3	33	33	30	1.926
SC-1	T50	GE223 processing Rhenium loaded 6.74% by wt.	2	2	3	33	33	30	1.99
SC-2	T50	GE223 processing Rhenium loaded 10.92% by wt.	2	2	3	33	33	30	2.04
114	T50		1	1	4	23	23	30	1.87
GE115	T50	CVD + pitch	1	1	5	30	30	30	1.86
MDAC 226(533)	T50	Low pressure pitch/CVD/final high pressure pitch	2	2	6	33	33	58	1.97
MDAC 226(534)	T50	Low pressure pitch/CVD/final low pressure pitch	2	2	6	33	33	58	1.95
MDAC 1-1-1-5	T50	Pitch/CVD/pitch	4D weave						1.98
MDAC 1-1-1-13	T75	Pitch/CVD/pitch	1	1	13	40	40	22	1.96
869	BM-1000/3000 (PAN)		Fine weave pierced fabric						1.953

Hexagonal geometry:  
33 mills between 37  
parallel lateral fibers

\* Preform dimensions for ideal conditions; not measured values from specimens examined.

\*\* Approximate values since billet-to-billet variations occur as well as spatial differences within a billet.

FIGURE CAPTIONS

- Fig. 1. Effects of 1 mm glass spheres impacting ATJ-S graphite ( $\sim 300 \text{ ms}^{-1}$ ).
- Fig. 2. A photographic sequence of a 1 mm Nylon sphere impacting ATJ-S graphite at  $2000 \text{ ms}^{-1}$ .
- Fig. 3. A schematic of the temporal development of the spalled region for ATJ-S graphite.
- Fig. 4. A schematic of the penetration dynamics after the formation of the spalled region.
- Fig. 5. A schematic of the penetration of ATJ-S graphite by a tungsten carbide sphere.
- Fig. 6. A photographic sequence of ATJ-S graphite impacted by a 1 mm Nylon sphere at  $2000 \text{ ms}^{-1}$ .
- Fig. 7. A photographic sequence for 223 carbon-carbon impacted by (a) a 1 mm Nylon sphere at  $2440 \text{ ms}^{-1}$ , (b) a 1 mm glass sphere at  $2400 \text{ ms}^{-1}$ .
- Fig. 8. A sequence showing the early stages of the impact depicted in Fig. 7b.
- Fig. 9. Distance-time curves for plume spreading in 223 carbon-carbon, after impacts by glass or Nylon spheres.
- Fig. 10. Expansion of spray diameter, 1 mm glass sphere impact at  $3200 \text{ ms}^{-1}$ .
- Fig. 11. Measurements obtained from high speed photographs in Fig. 7a.
- Fig. 12. An optical overview of the damage to 223 carbon-carbon impacted at  $3700 \text{ ms}^{-1}$  by a 1 mm glass sphere, (a) polished, (b) polymer impregnated and polished.
- Fig. 13. Scanning electron micrographs of the damage on the impact surface on 223 material created by 1 mm glass projectiles, (a) a  $1300 \text{ ms}^{-1}$  impact showing the retained projectile, (b) a  $2000 \text{ ms}^{-1}$  impact showing a larger central

damage zone, (c) a  $2700 \text{ ms}^{-1}$  impact showing the formation of the outer ledge, (d) an enlargement of (a) showing the fragmentation of the glass projectile, (e) a further enlargement of (a) showing the accommodation of the projectile by the target material.

- Fig. 14. Scanning electron micrographs of a high velocity ( $6,000 \text{ ms}^{-1}$ ) impact on 223 material illustrating (a) the surface stripping of the lateral fibers, (b) the formation of the central penetration zone and the outer ledge zone of the crater.
- Fig. 15. A scanning electron micrograph of a  $4,000 \text{ ms}^{-1}$  impact on 223 material illustrating the accommodation damage at the base of the central penetration zone.
- Fig. 16. Overview scanning electron micrographs of composites impacted by 1 mm glass sphere at  $6000 \text{ ms}^{-1}$ , (a) 2-2-3, (b) 1-1-5, (c) 1-1-13.
- Fig. 17. Scanning electron micrographs of damage details, (a) lateral fiber bundle kinking in 115, (b) fractured fibers observed on the longitudinal bundles in the outer ledge.
- Fig. 18. Impact damage on 223 material created by deformable projectiles, (a) 1 mm Nylon projectiles at  $2700 \text{ ms}^{-1}$ , (b) water drop at  $4000 \text{ ms}^{-1}$ , (c) three adjacent water drops at  $4000 \text{ ms}^{-1}$  showing the linking between damage zones.
- Fig. 19. Scanning electron micrographs of the damage created in 115 material by a 1 mm glass projectile at  $3600^\circ\text{C}$  and  $6000 \text{ ms}^{-1}$ , (a) a general view, (b) a localized view of the distorted ends of the longitudinal fibers in the central zone, (c) a view of the permanent separation between fiber bundles at the crater periphery.
- Fig. 20. A schematic of a section near the impact center through longitudinal fiber bundles.

- Fig. 21. A schematic of an adjacent section through lateral fiber bundles.
- Fig. 22. A schematic of sections near the crater periphery, (a) through lateral bundles, (b) through longitudinal bundles.
- Fig. 23. Polarized reflected light micrographs of kinked longitudinal fibers beneath the impact center in 114 material, (a,b) zones immediately adjacent to the crater surface, showing fracture as well as kinking (c,d) zones just below the impact center showing intensive kinking, (e,f) zones at the periphery of the kinked region.
- Fig. 24. A schematic of the kink morphologies.
- Fig. 25. Polarized reflected light micrographs of kinked lateral fibers adjacent to the crater in 223 material.
- Fig. 26. Polarized reflected light micrographs of the lateral fiber damage created under the impact center in 223 material.
- Fig. 27. Lateral fiber fractures in 223 material near the crater periphery, (a) a scanning electron micrograph of the uppermost lateral bundle, (b) a scanning electron micrograph of the second lateral bundle, (c) a reflected polarized light micrograph of a section through (a).
- Fig. 28. Longitudinal fiber fracture in 223 material near the crater periphery, (a) a reflected polarized light micrograph of the zone just below the surface, (b) a scanning electron micrograph of a zone at a distance  $3d$  below the surface.
- Fig. 29. Polarized light micrographs of sections through a 223 material impacted by a 1 mm glass projectile at  $2400 \text{ ms}^{-1}$ , (a) lateral fiber bundles beneath the impact center, (b) a kink in a lateral fiber bundle, (c) kinks in a longitudinal fiber bundle directly beneath the impact center.

- Fig. 30. A reflected polarized light micrograph, of a section through the center of impact, for a 223 material impacted at 3600°C by a 1 mm glass projectile at 4000 ms<sup>-1</sup>.
- Fig. 31. Polarized light micrographs of a section through a 223 material impacted at 3600°C by a 1 mm glass projectile at 4000 ms<sup>-1</sup>, (a) overview near the base of the crater, (b) a region to the side of the central zone, (c) a region beneath the central zone.
- Fig. 32. Higher magnification view of kinks from the sample depicted in Fig. 31, showing that (a) large localized distortions are accompanied by deformation and fracture, and (b) smaller distortions can occur without fracture.
- Fig. 33. Polarized light micrographs of the sample depicted in Fig. 31, showing (a) complex kinking and distortion, and (b) kinking and fracture beneath the impact center.
- Fig. 34. Quasi-static indentation damage, (a) a polarized light reflected micrograph of a section showing kinking and fracture of longitudinal bundles, (b) a scanning electron micrograph of the impression, (c) a scanning electron micrograph of (b) but with the top layer of the impression removed by immersion in a ultrasonic bath.
- Fig. 35. The dynamic penetration pressure for 223 at room temperature.
- Fig. 36. The temperature dependence of the dynamic hardness for 223 compared with the mass loss ratio.
- Fig. 37. The relation between the mass loss and the dynamic hardness for several carbon-carbon materials in the virgin and surface obscured conditions.
- Fig. 38. A summary of compliance measurements on each zone of the composite.
- Fig. 39. The critical kinking stress as a function of the foundation modulus for a longitudinal fiber from 223 material.
- Fig. 40. A schematic of buckling on an elastic foundation and the resultant kink formation under compressive forces.

Fig. 41. A schematic of the buckling and kinking process, (a) the initial buckled configuration, (b) kink initiation by fiber fracture at the interface, (c) kink propagation by sequential fiber fracture.

Fig. 42. The deformation of a beam subjected to combined shear and tensile loading.

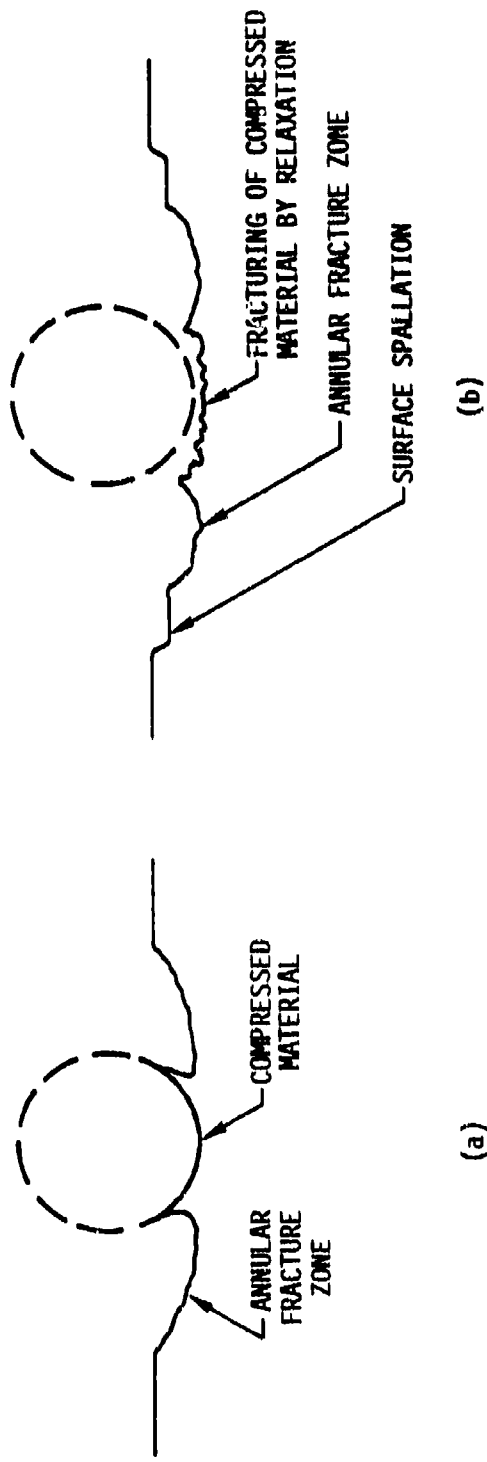


Fig. 1

1000 $\mu$ m Nylon Bead Impacting ATJ-S Graphite at 6 kfps

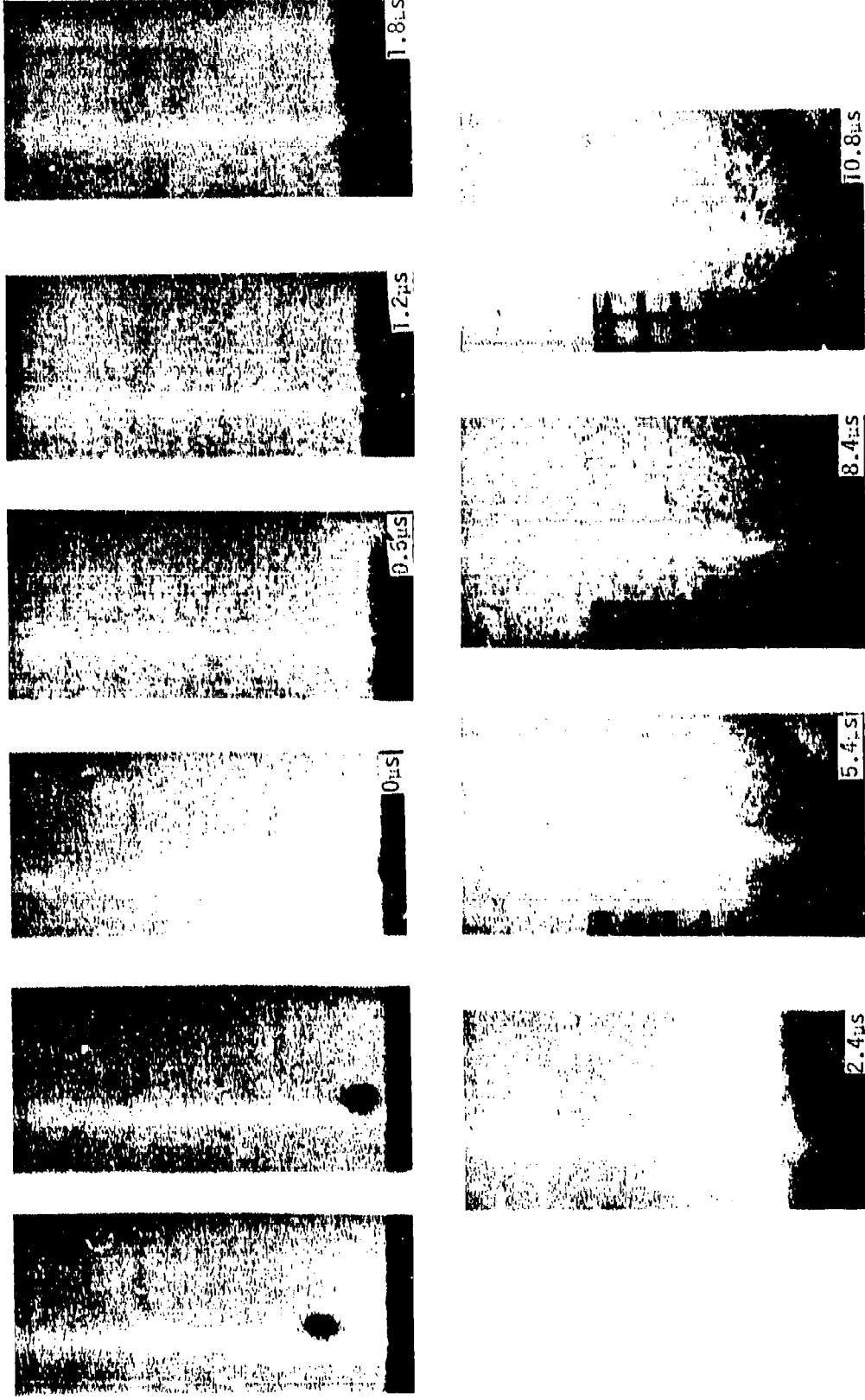


Figure 2

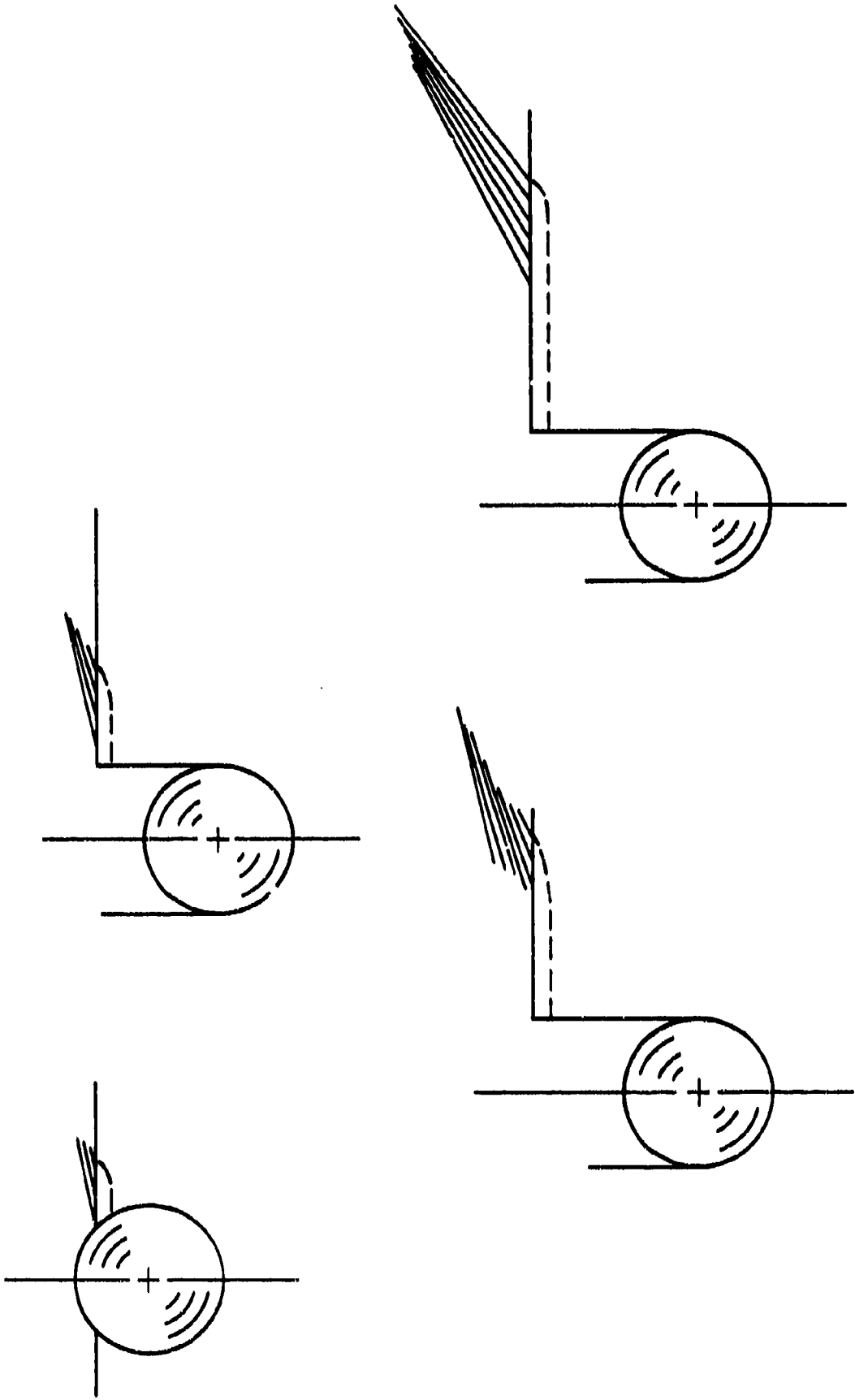
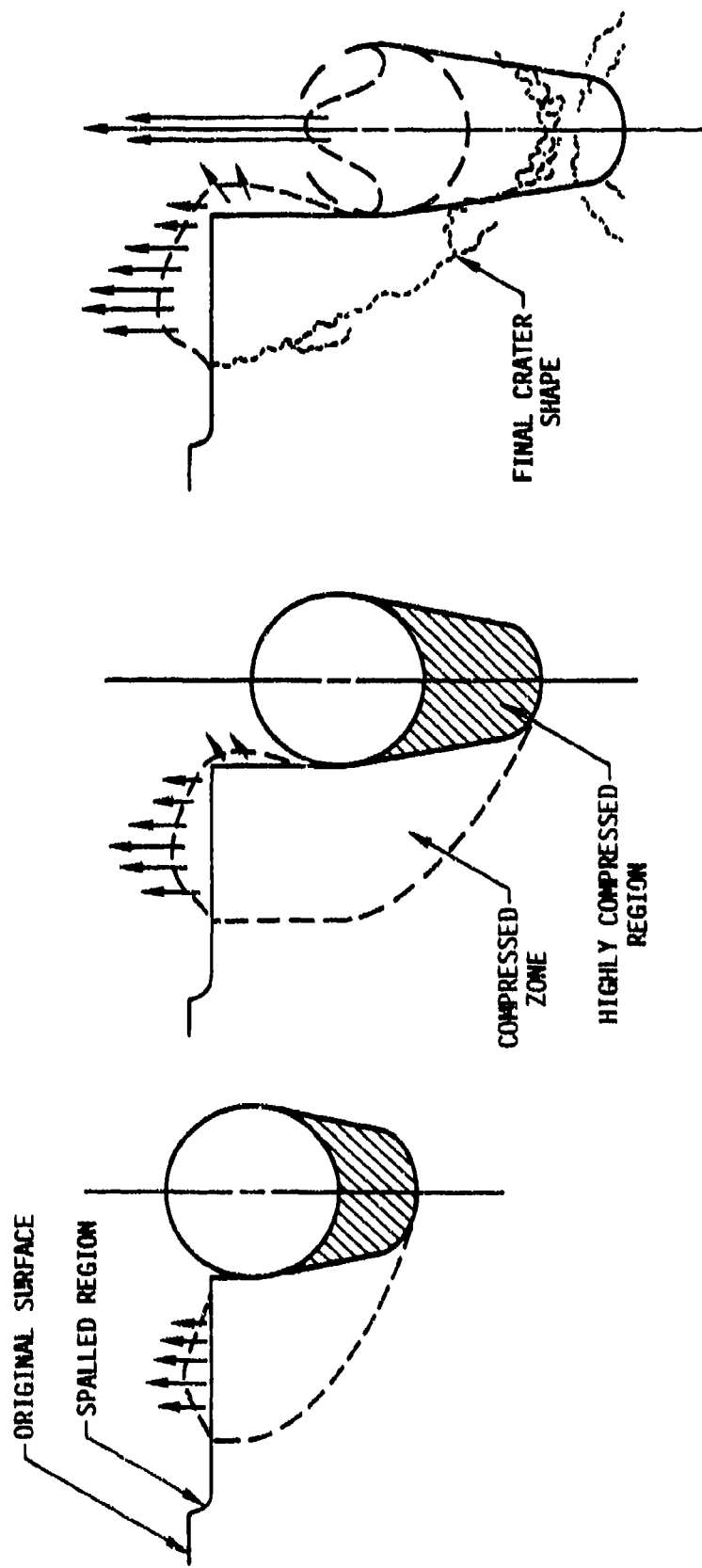


Fig. 3



PENETRATION DYNAMICS

Fig. 4

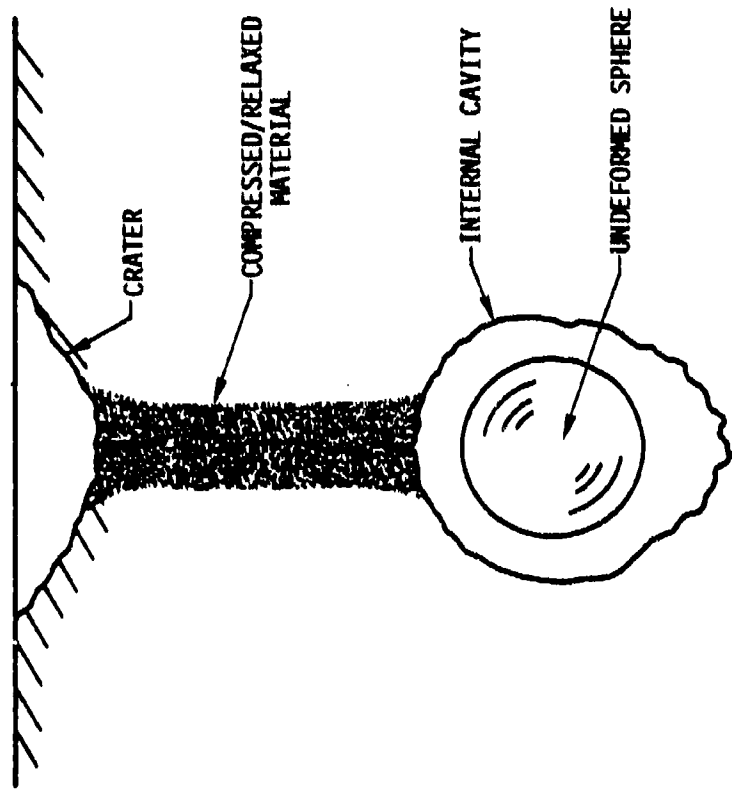


Fig. 5

1000 $\mu\text{m}$  Nylon Bead Impacting ATJ-S Graphite at 6 kfps

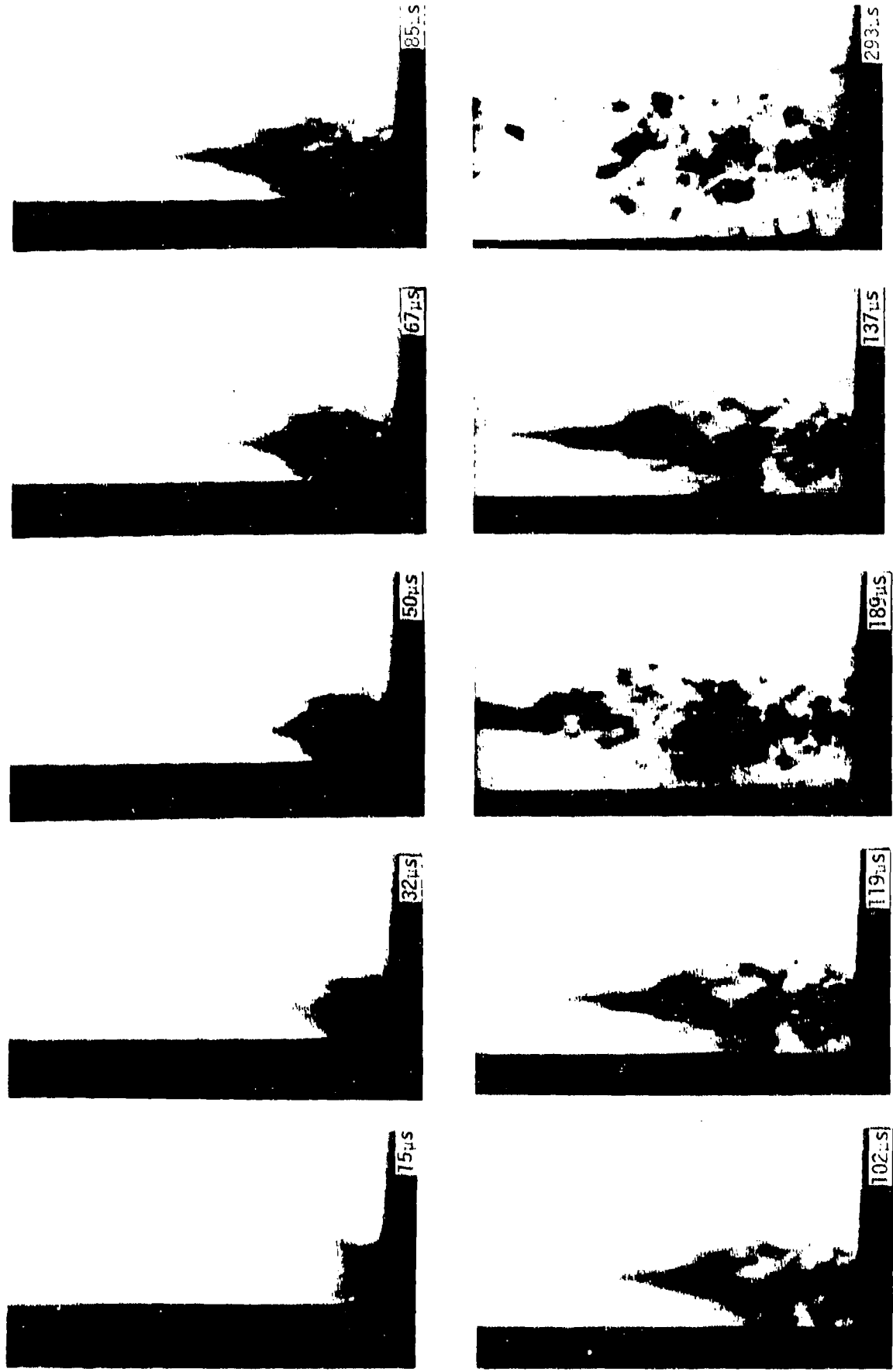
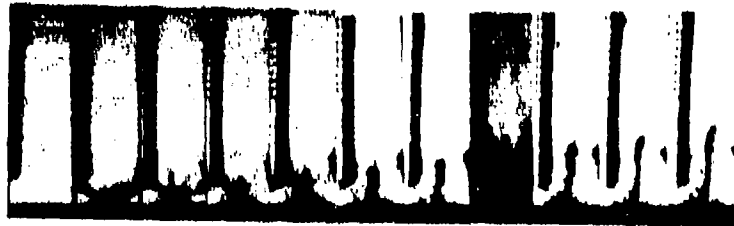


Figure 6



a



b

Figure 7



Figure 8

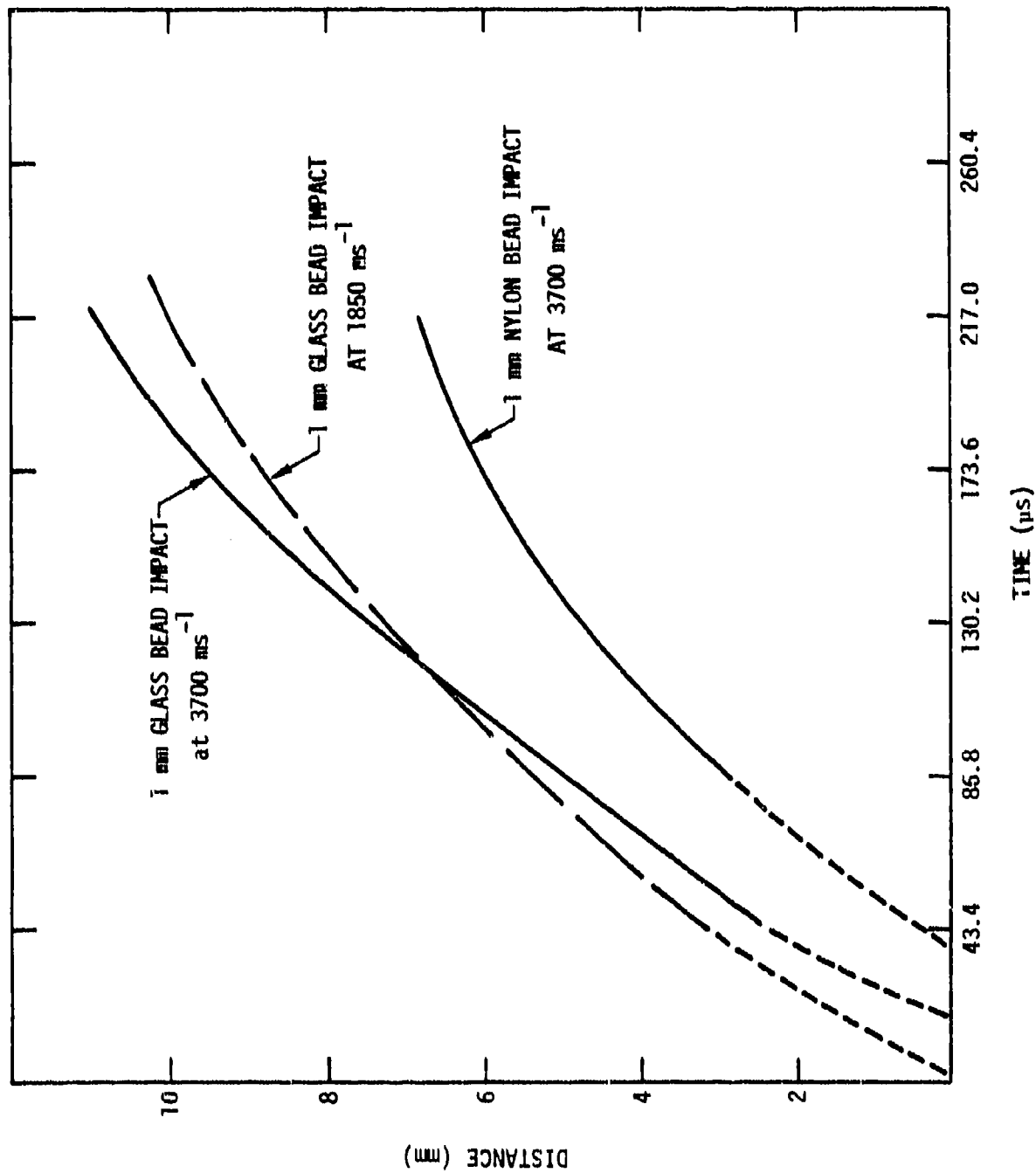


Fig. 9

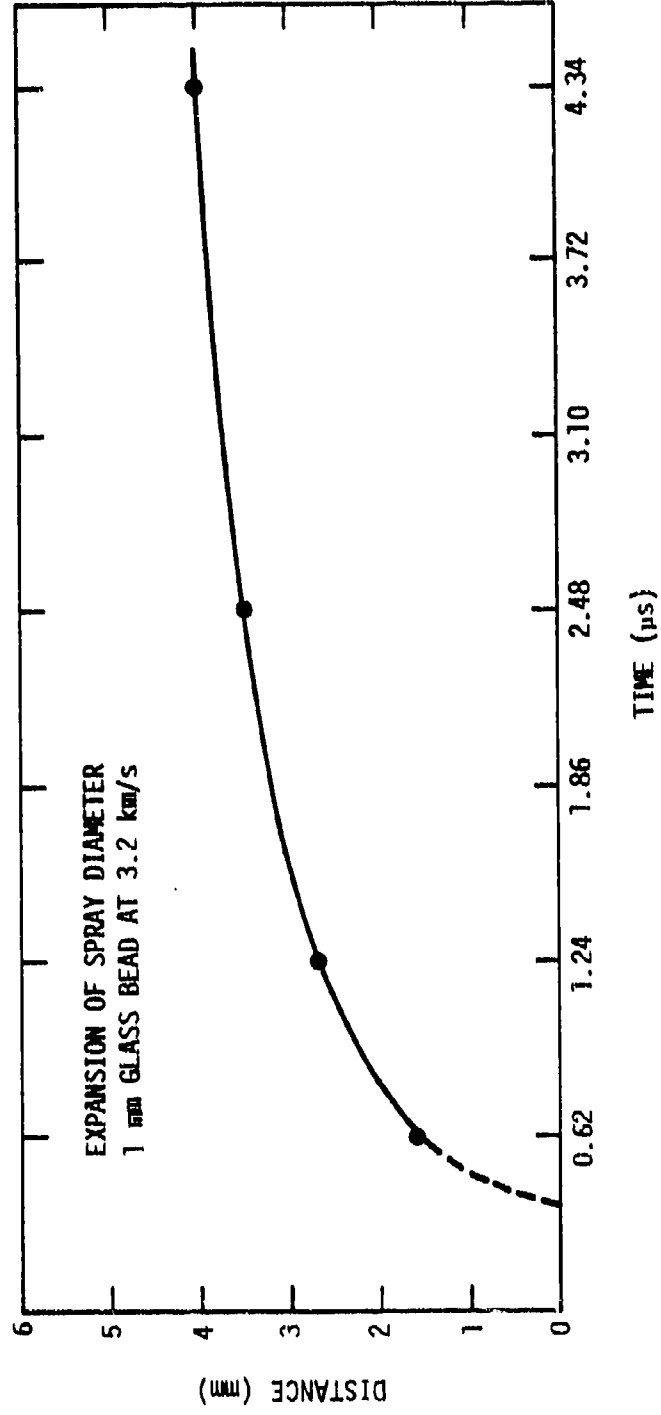


Fig. 10

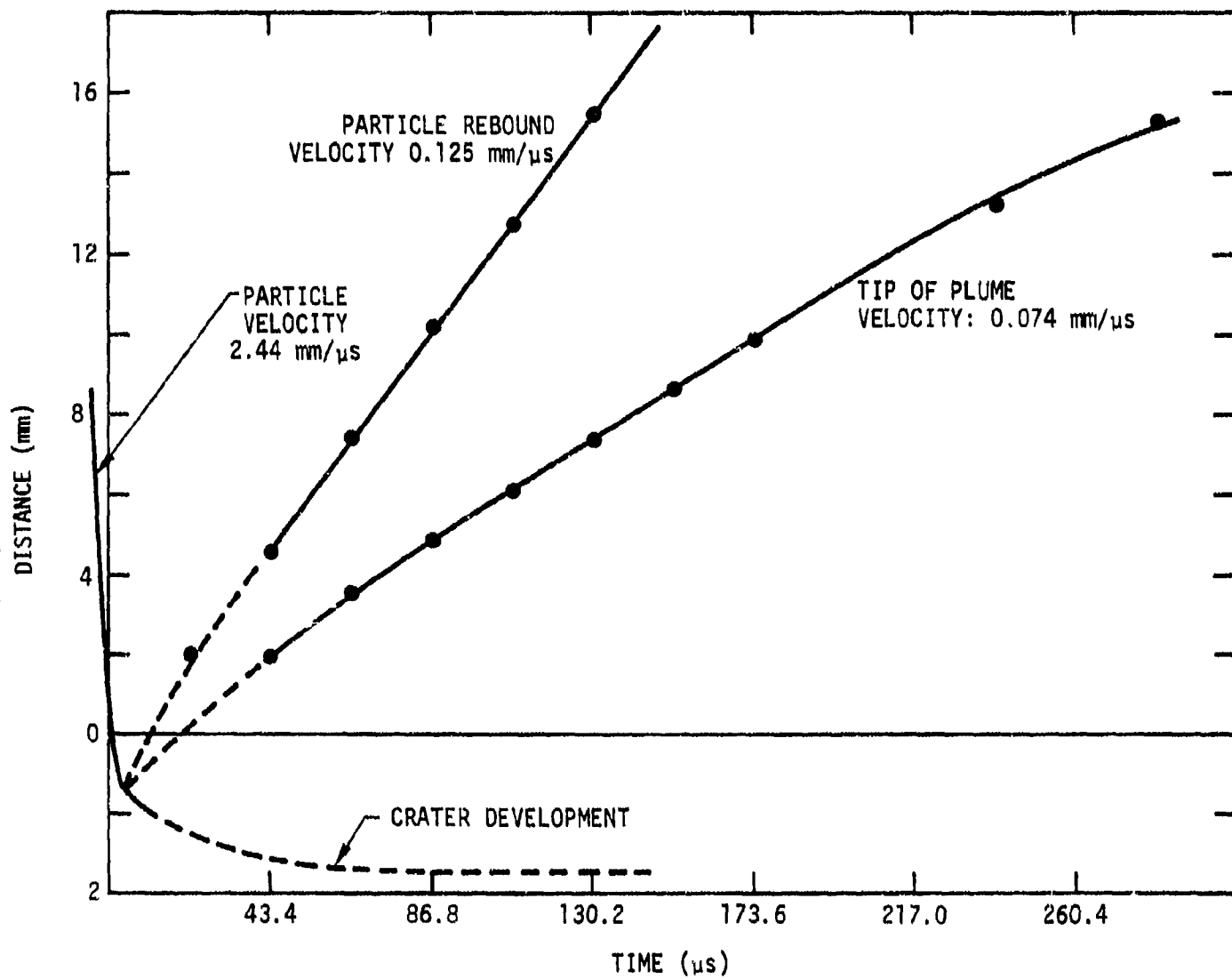


Fig. 11

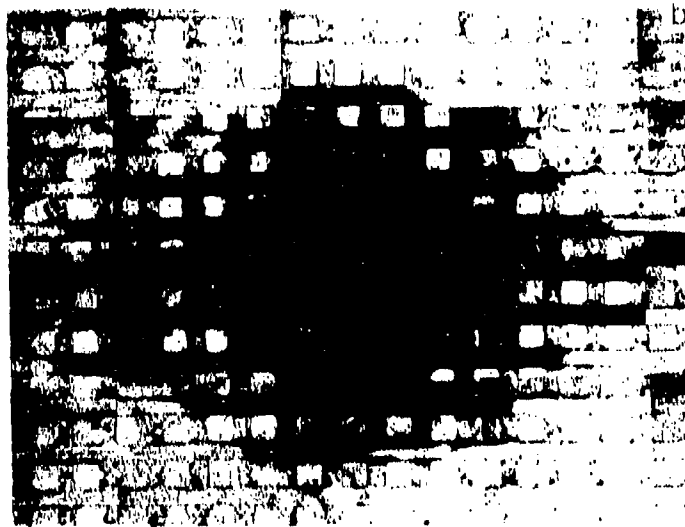
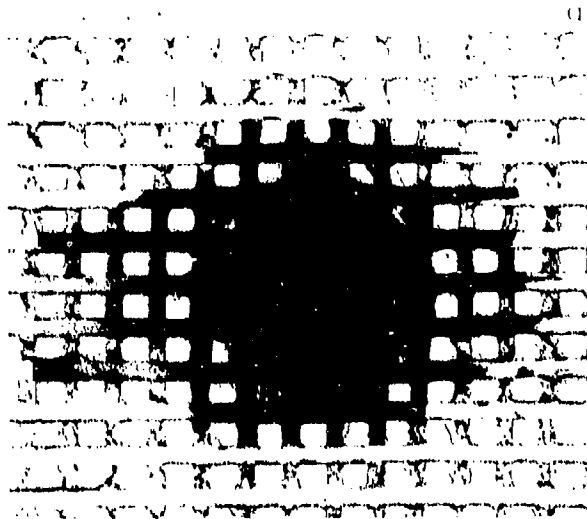


Figure 12

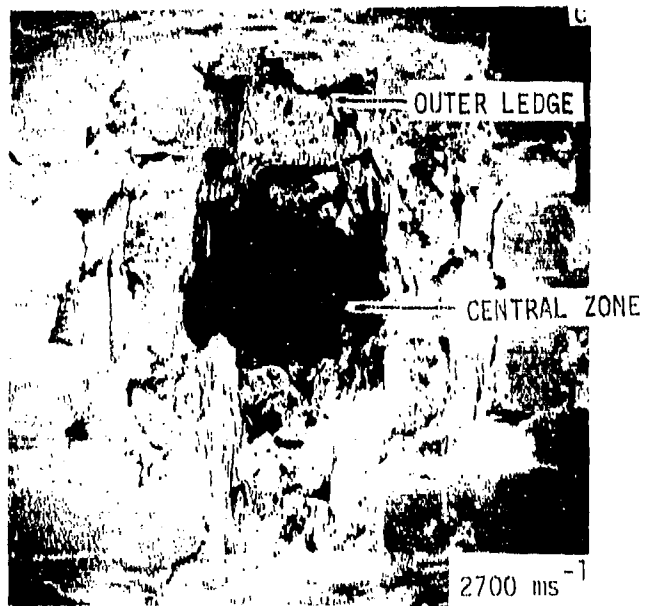
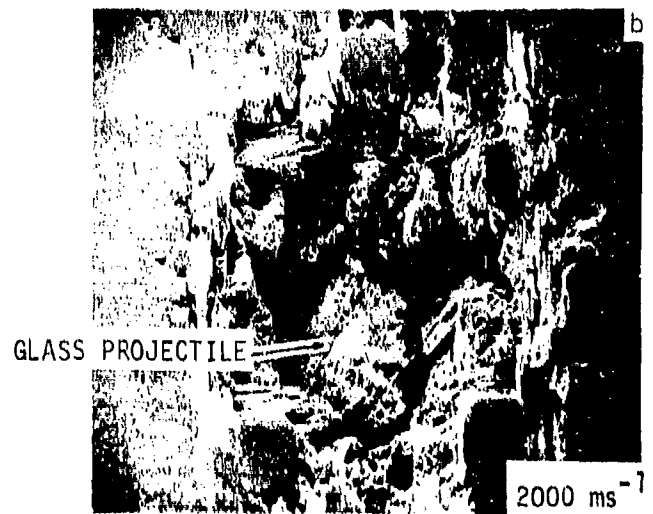
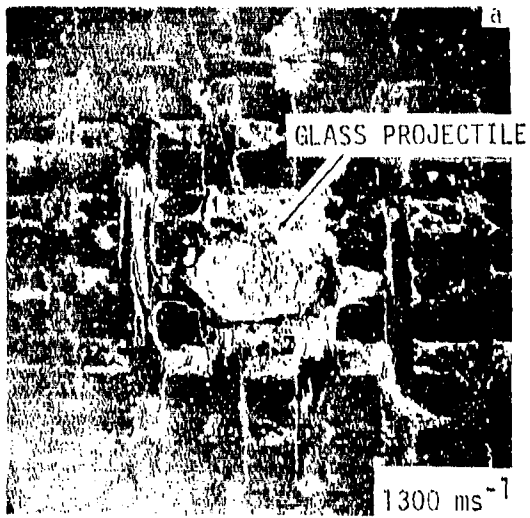


Figure 13

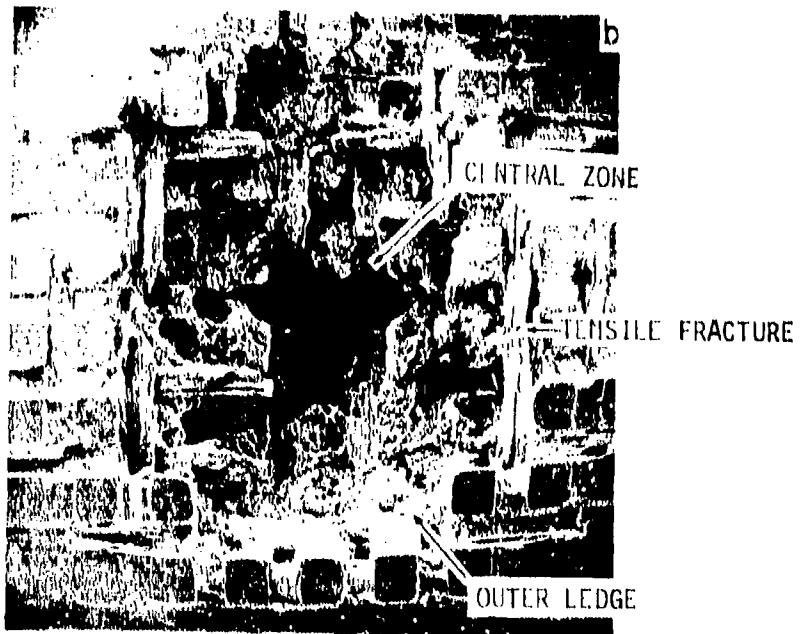
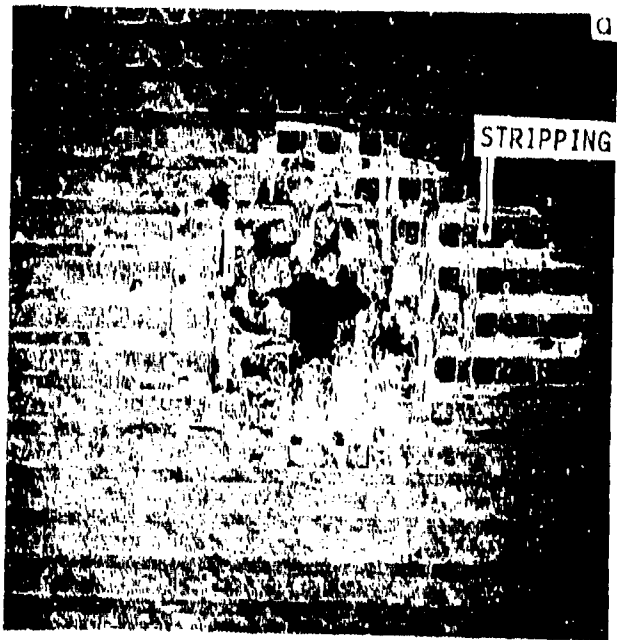


Figure 14



Figure 15

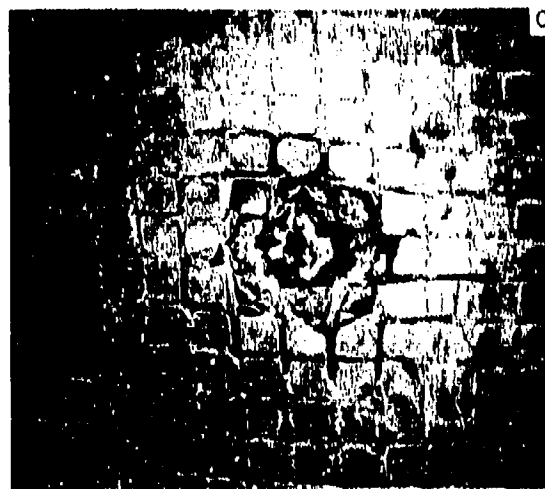
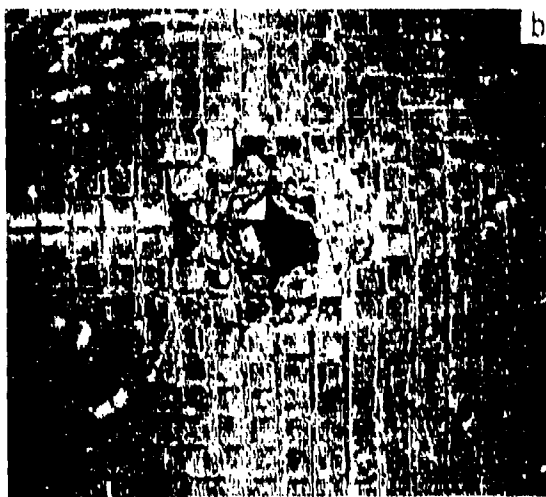
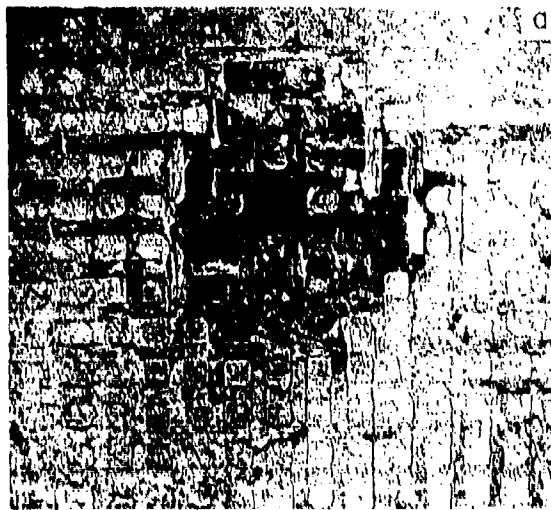


Figure 16



Figure 17

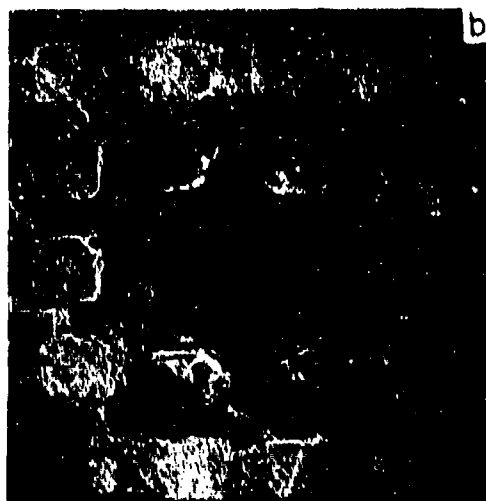
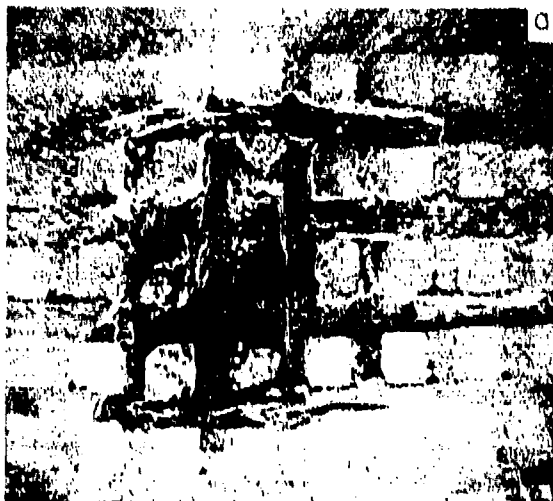


Figure 18

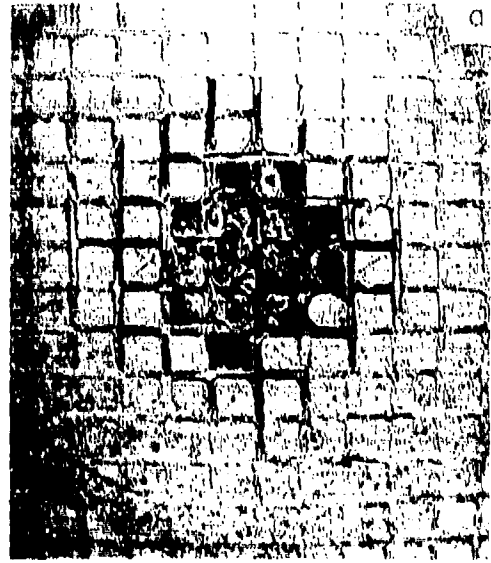


Figure 19

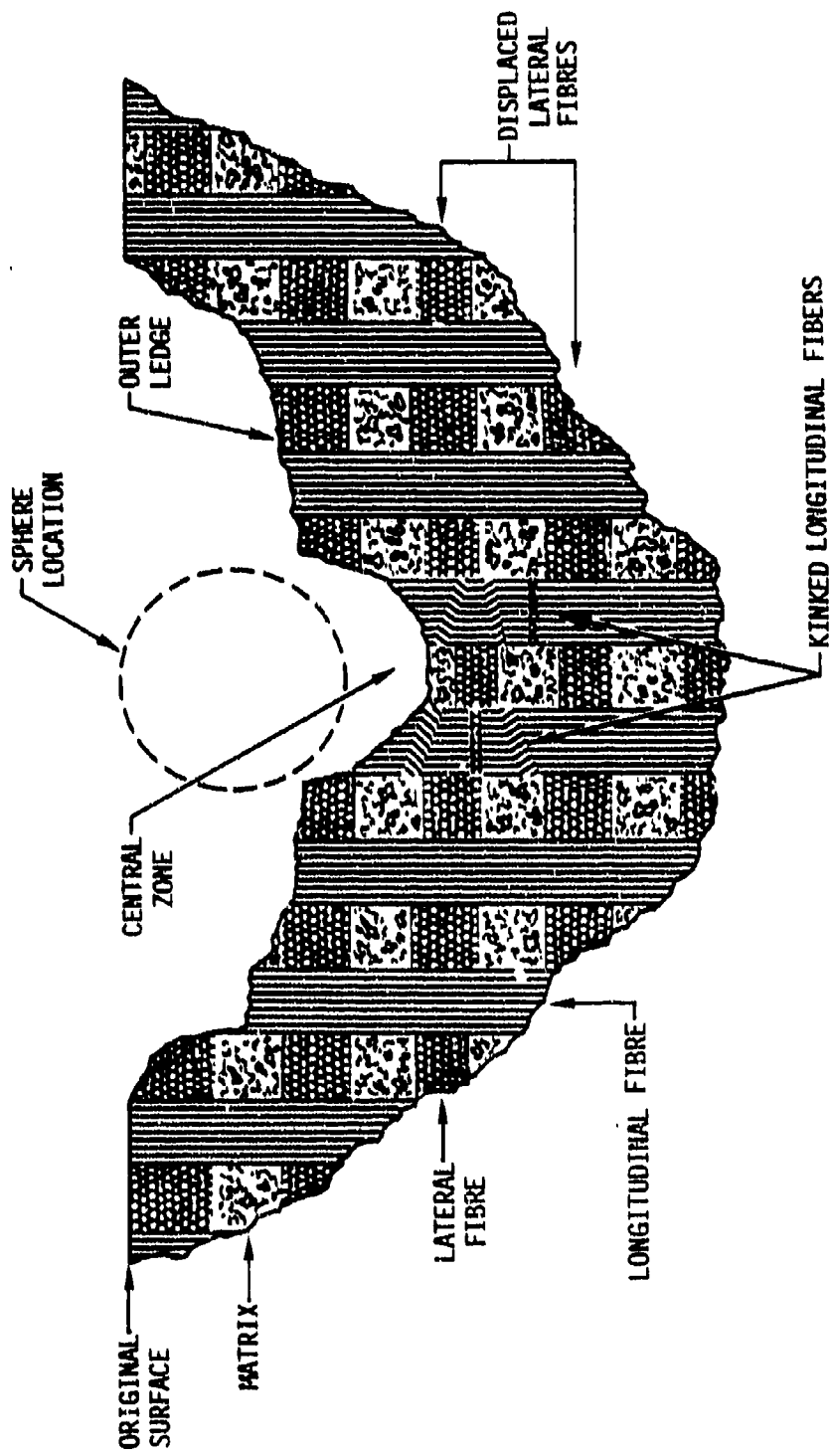


Fig. 20

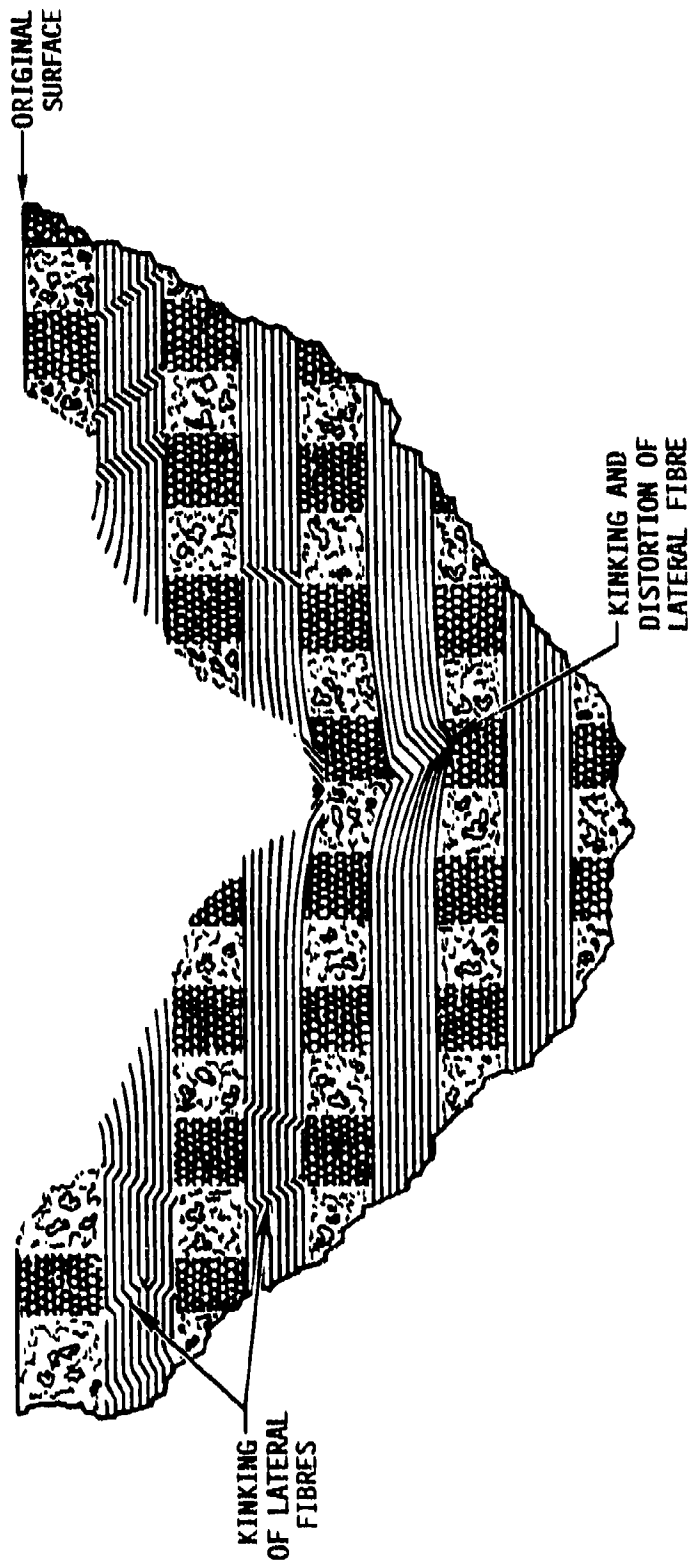
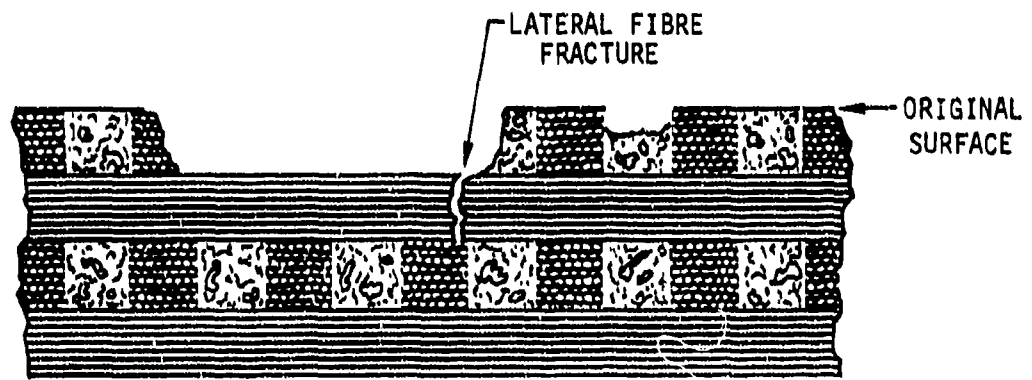
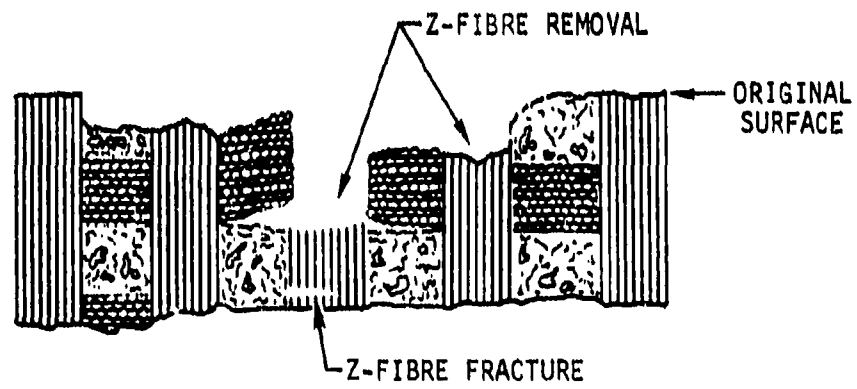


Fig. 21



(a)



(b)

Fig. 22

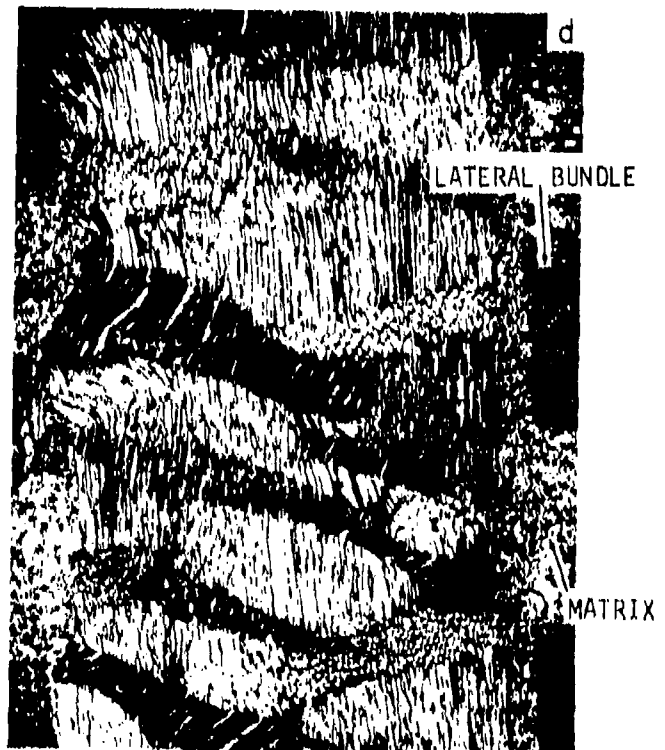


Figure 23

e  
KINK ARREST AT  
PRE-EXISTING VOID



f  
KINK ARREST AT  
KINK INTERSECTION



Figure 23

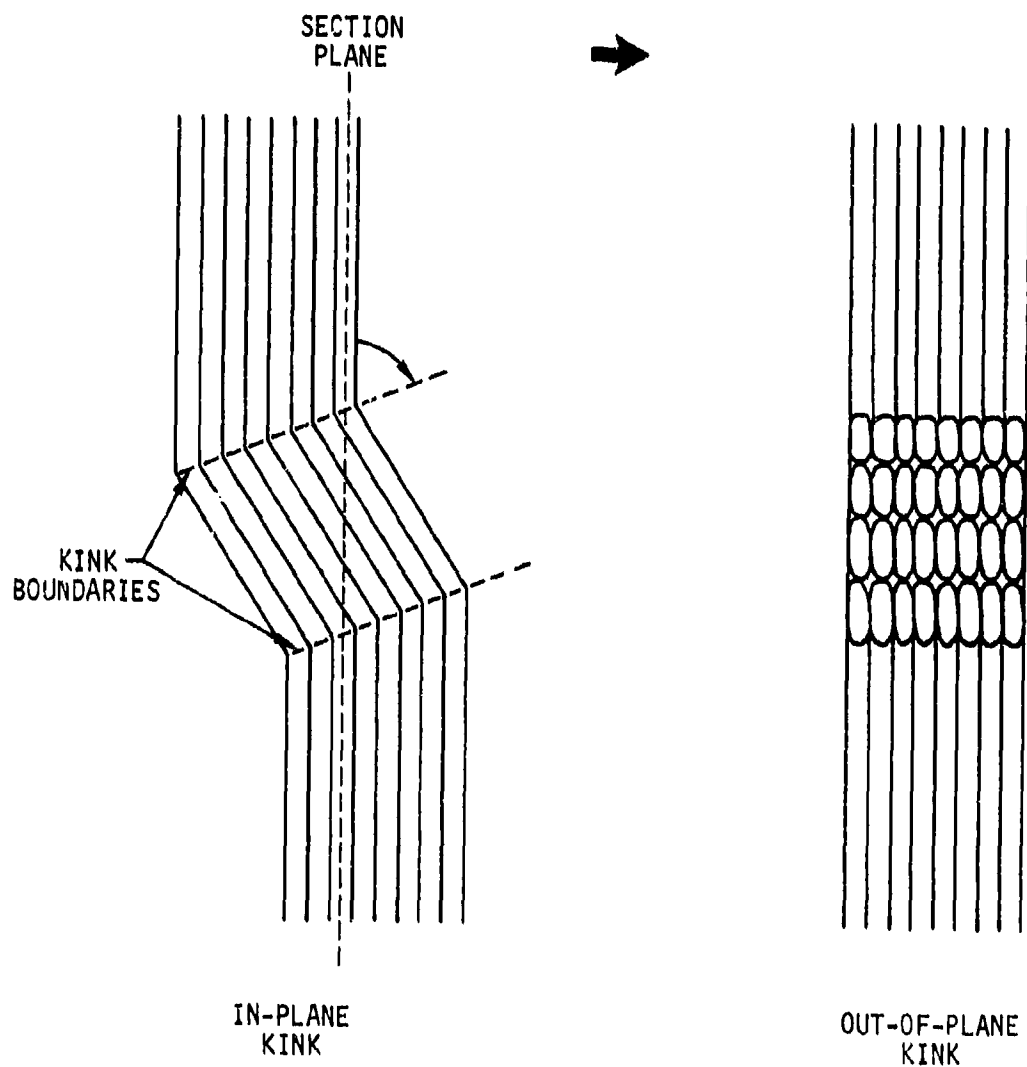


Fig. 24



Figure 25

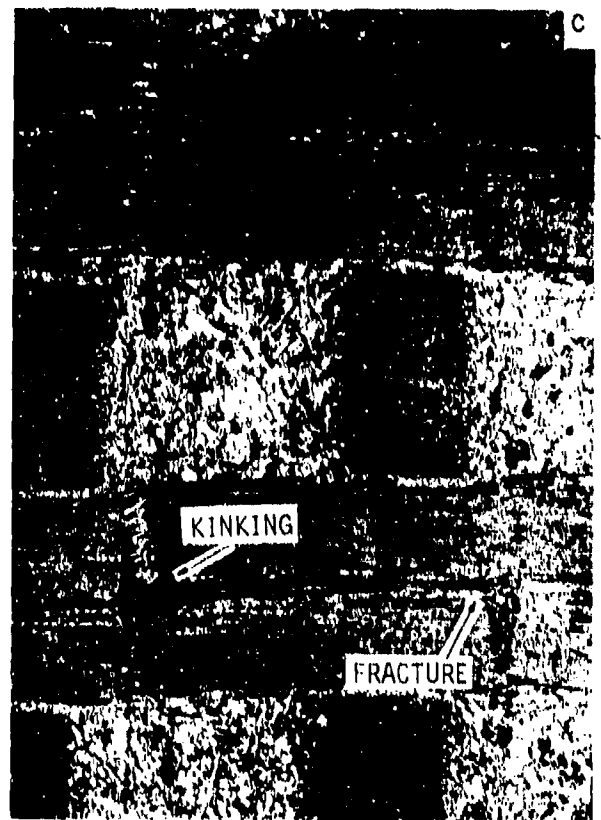
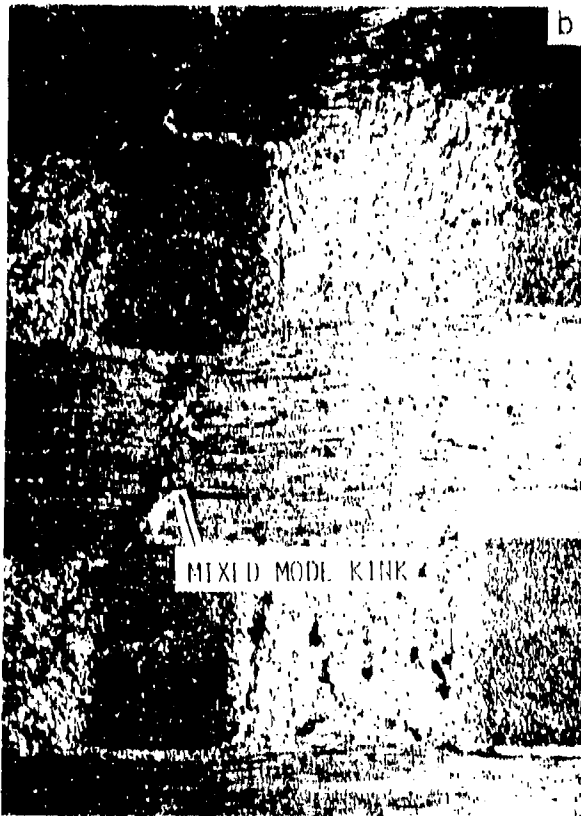


Figure 26



Figure 26

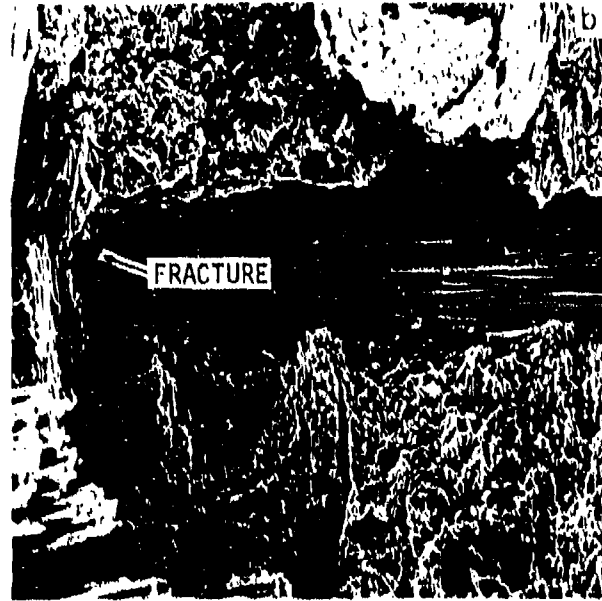


Figure 27

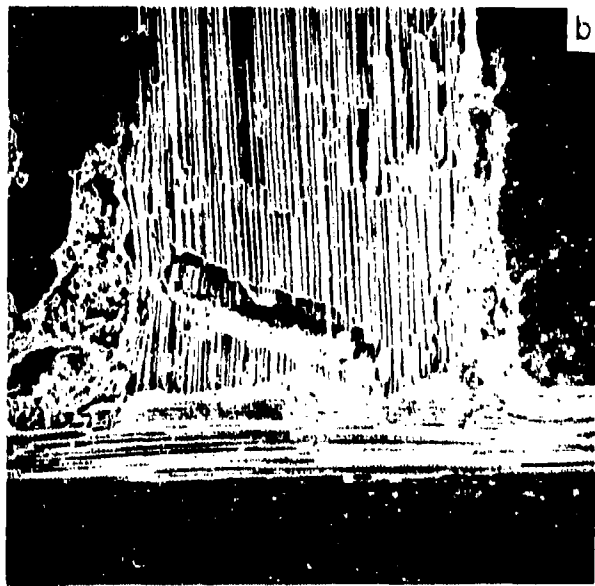
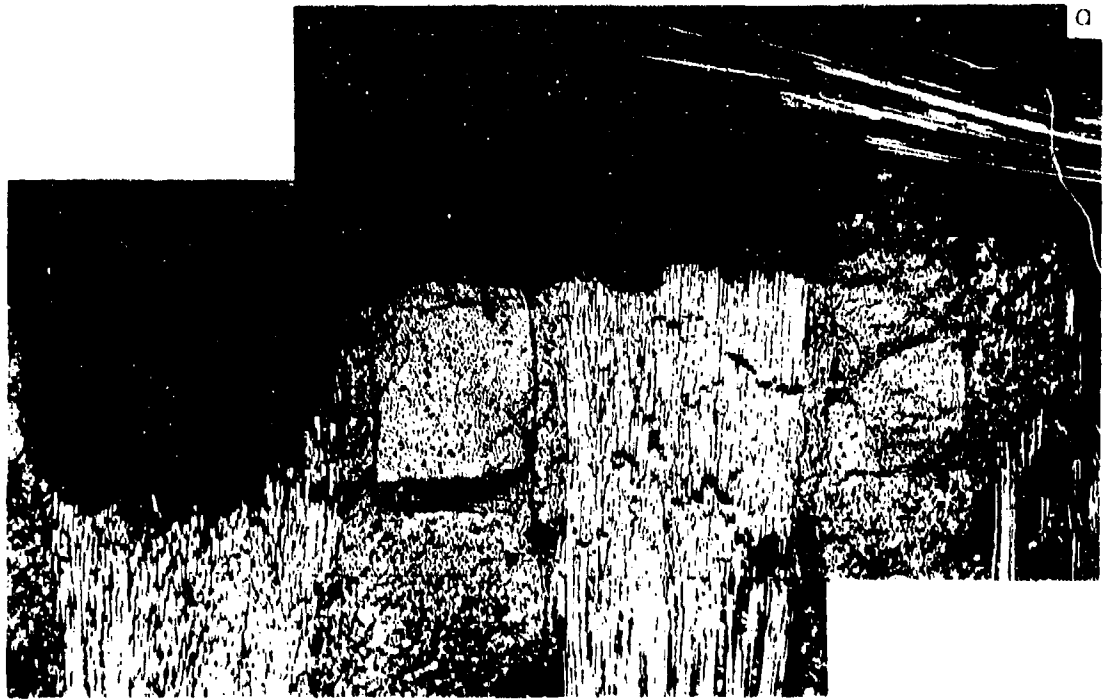


Figure 28

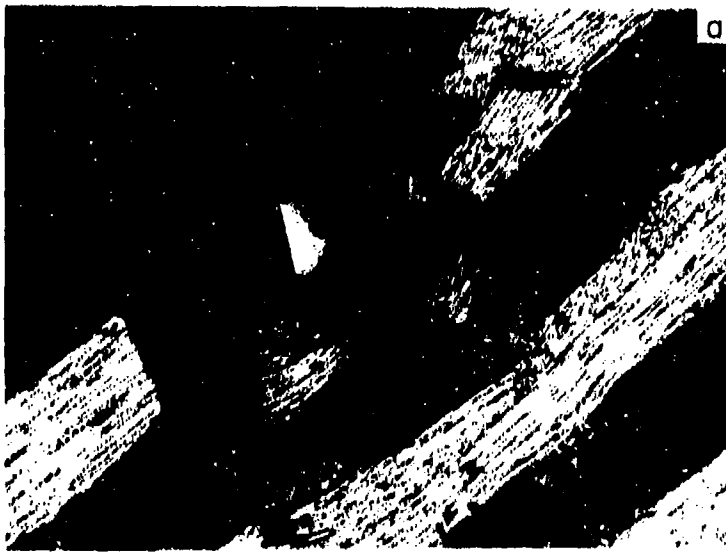


Figure 29



Figure 30



Figure 31



Figure 32

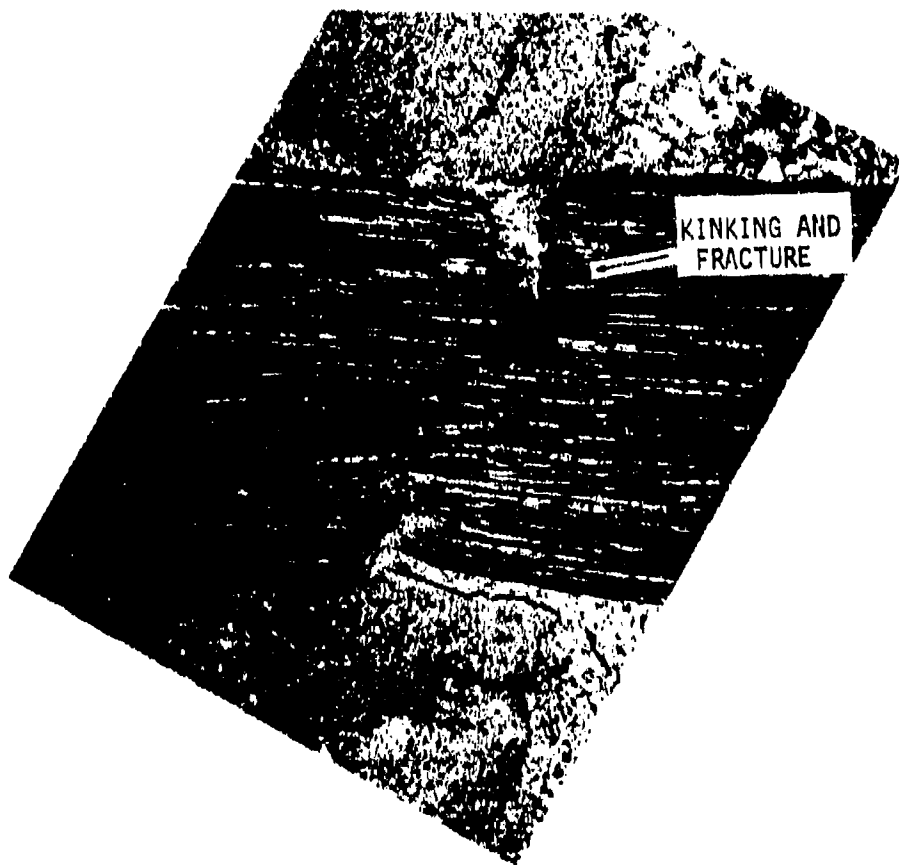
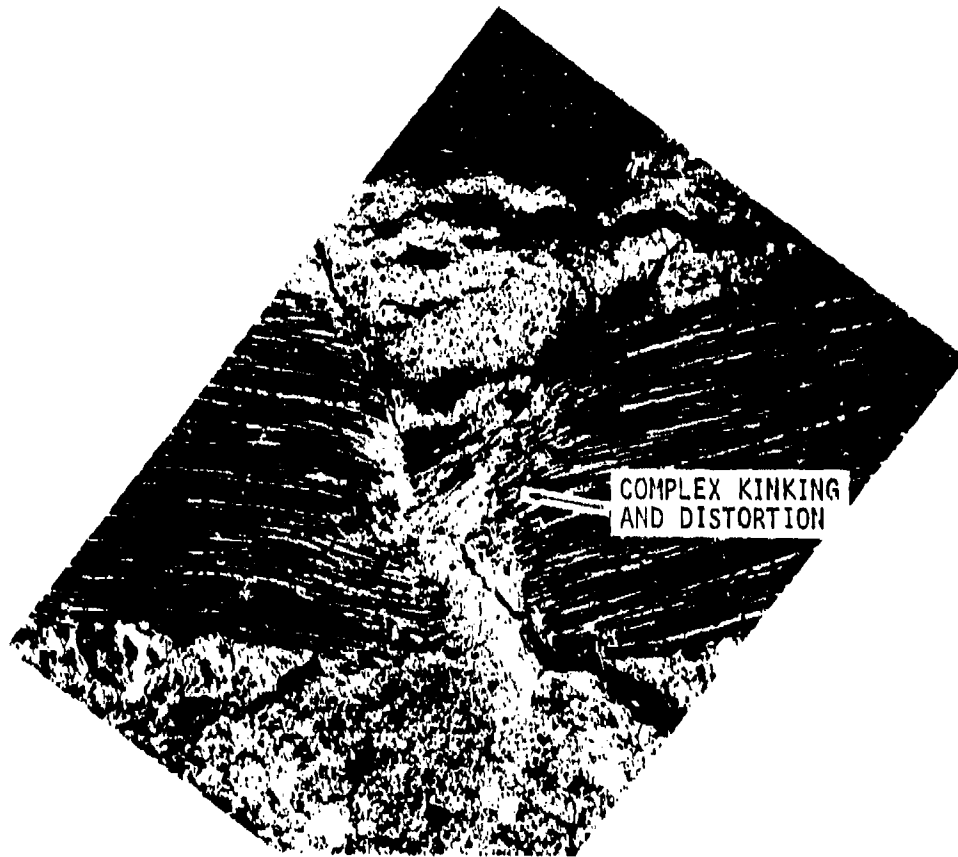


Figure 33

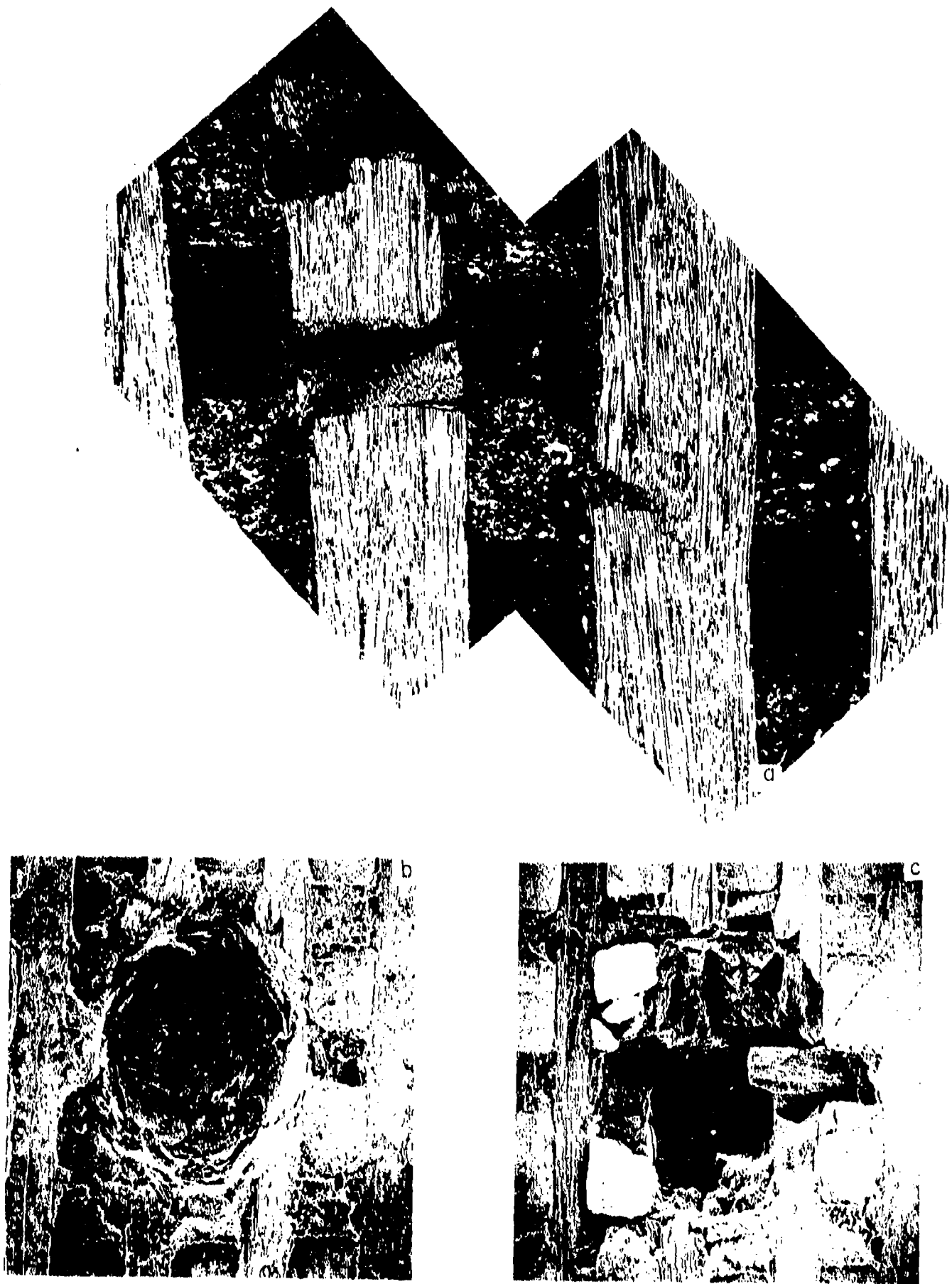


Figure 34

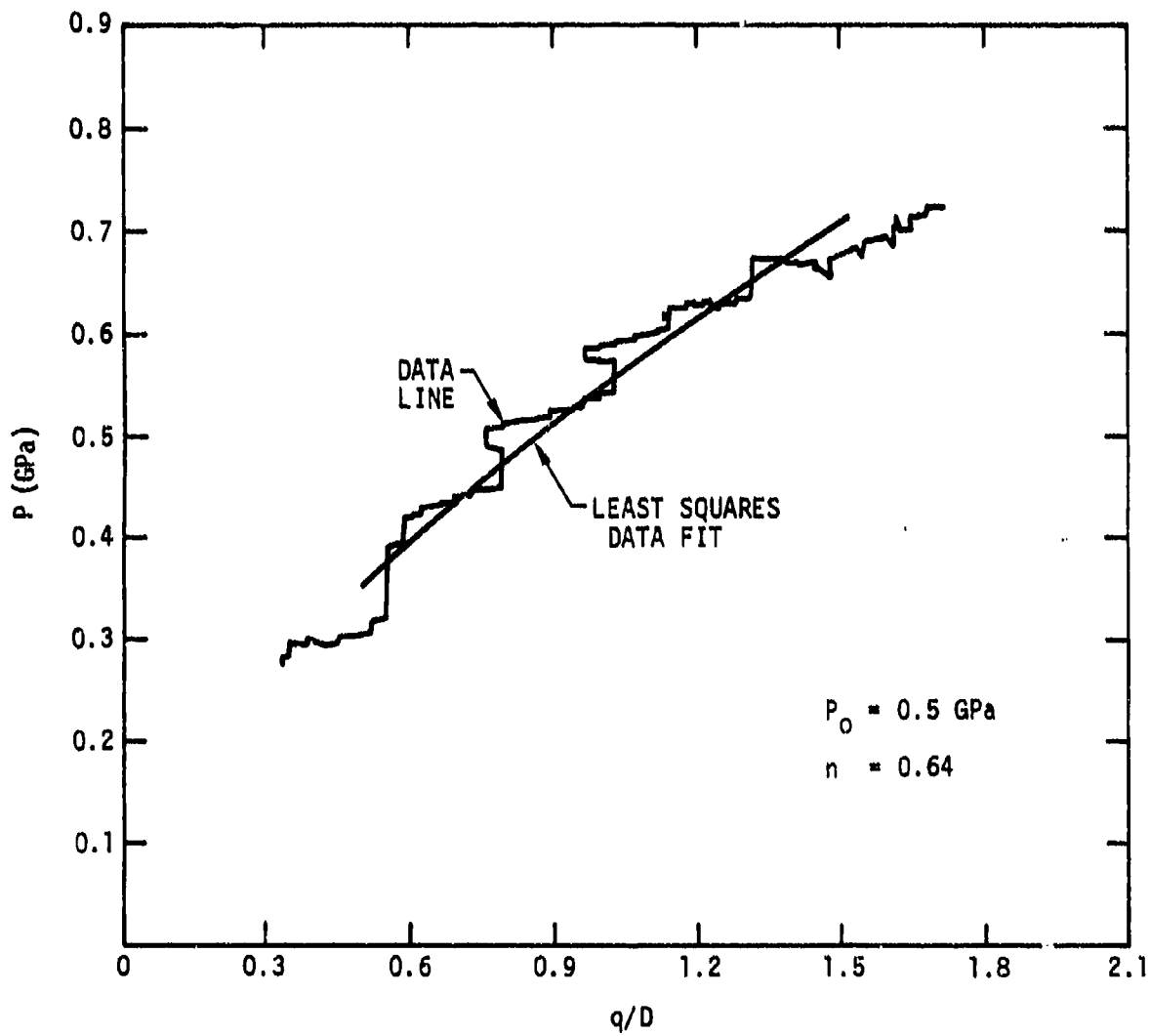


Fig. 35

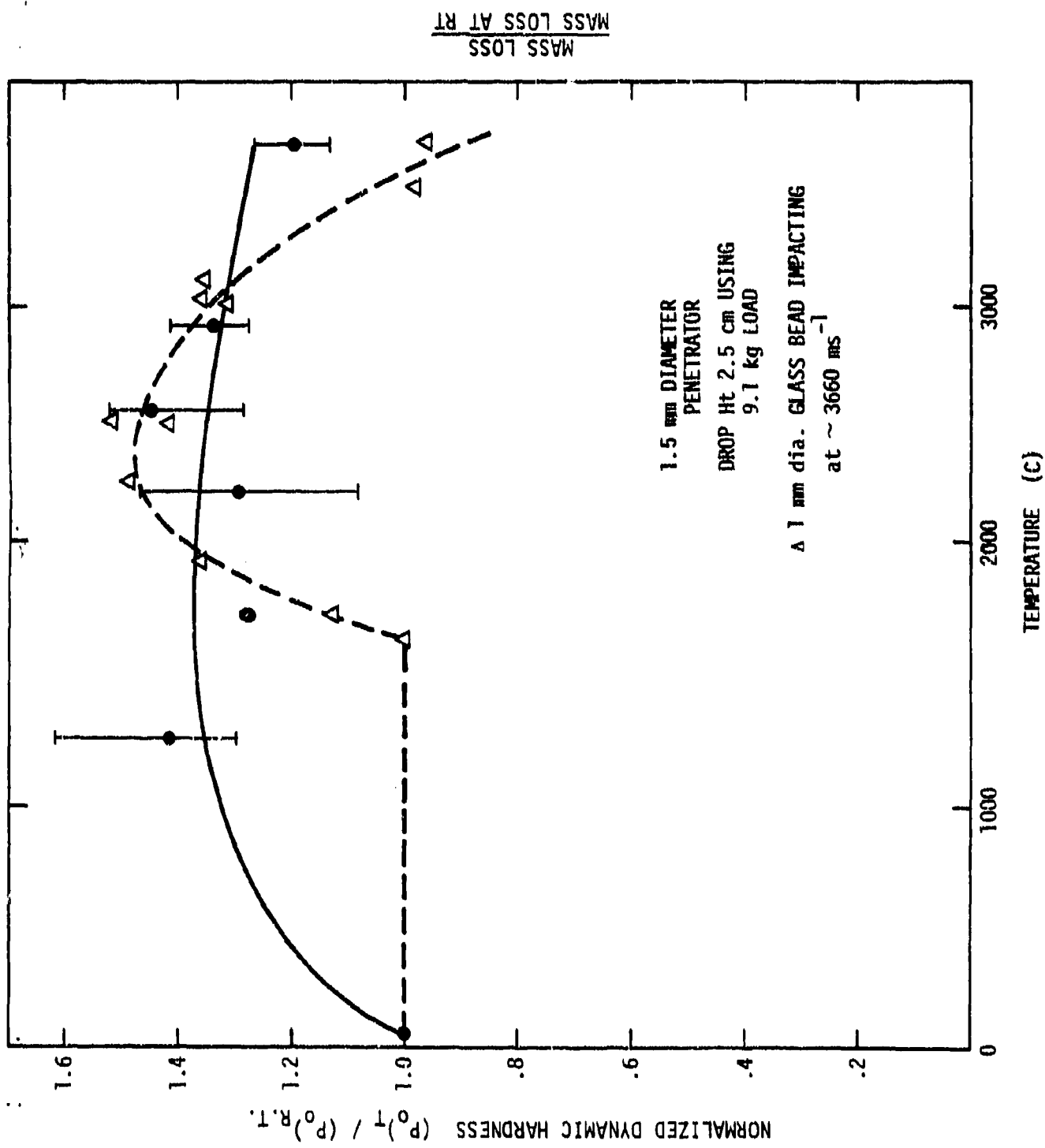


Fig. 36

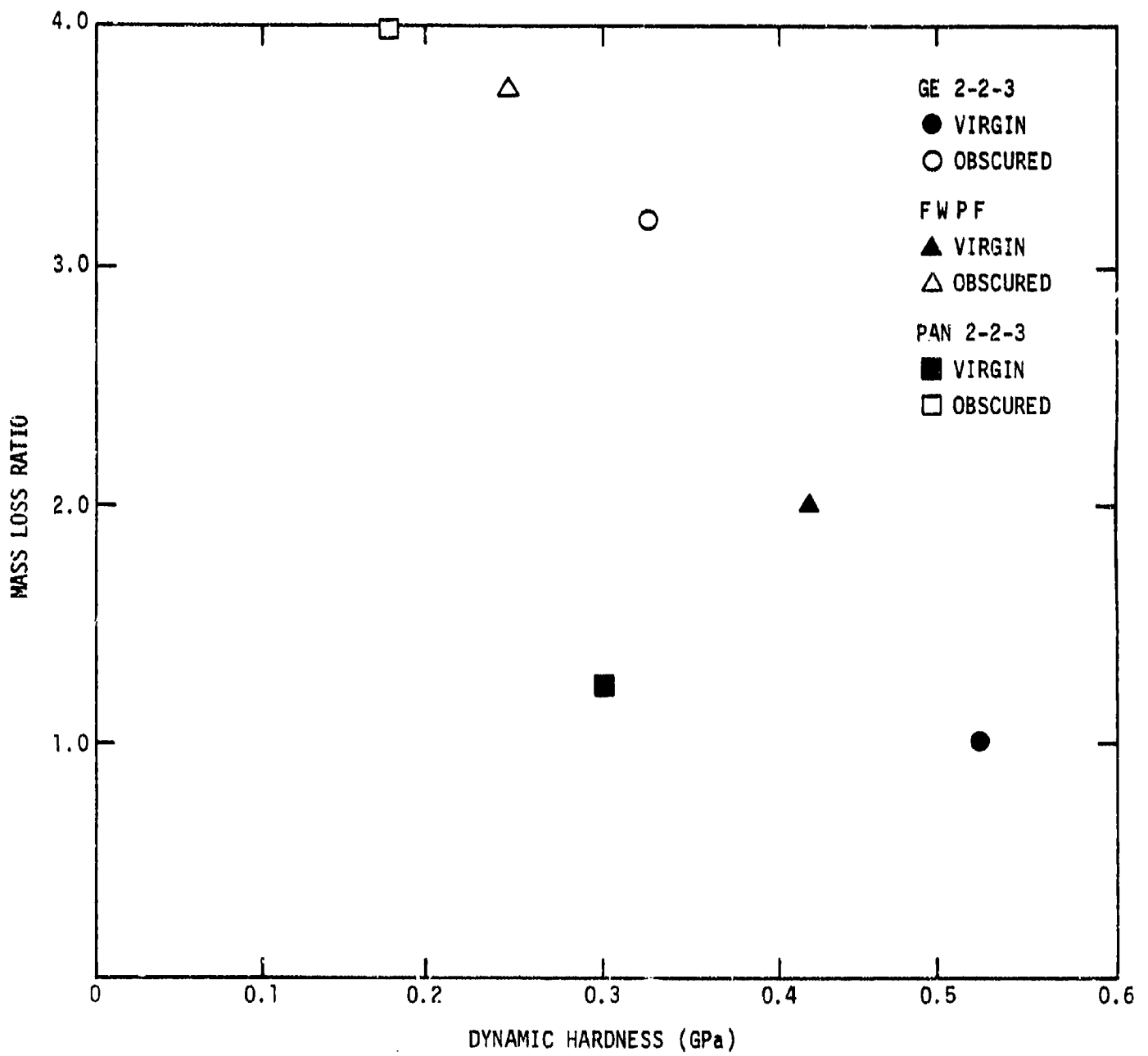


Fig. 37

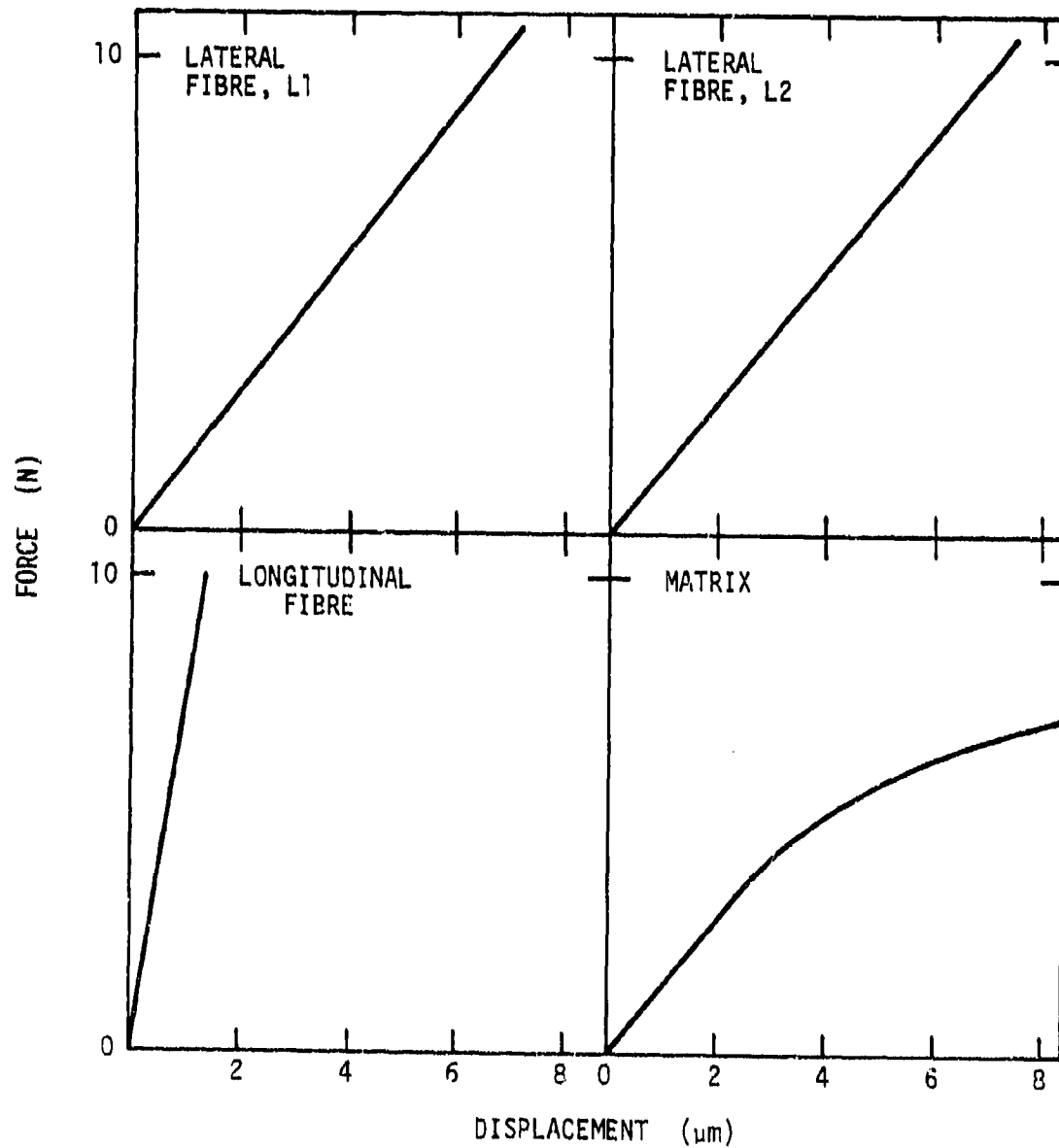
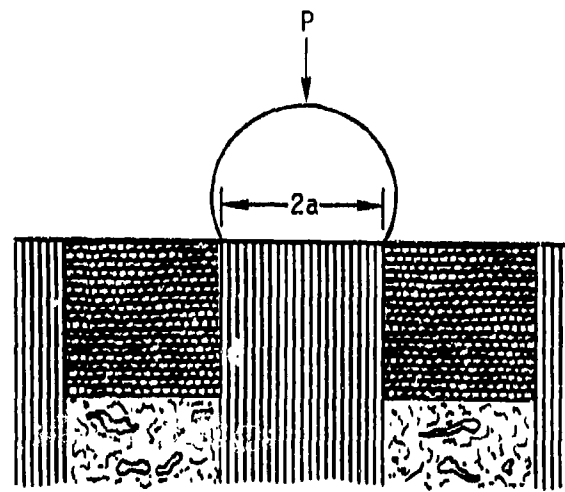


Fig. 38

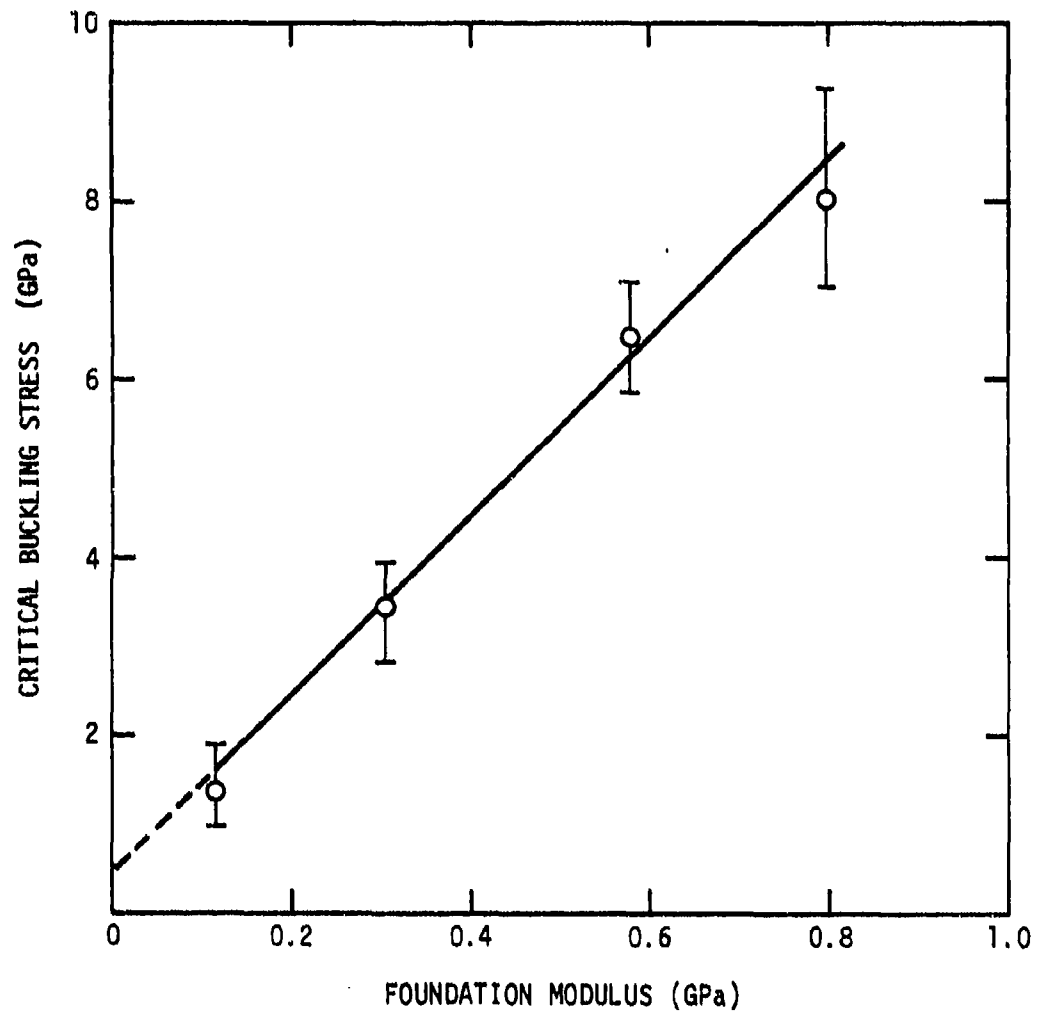


Fig. 39

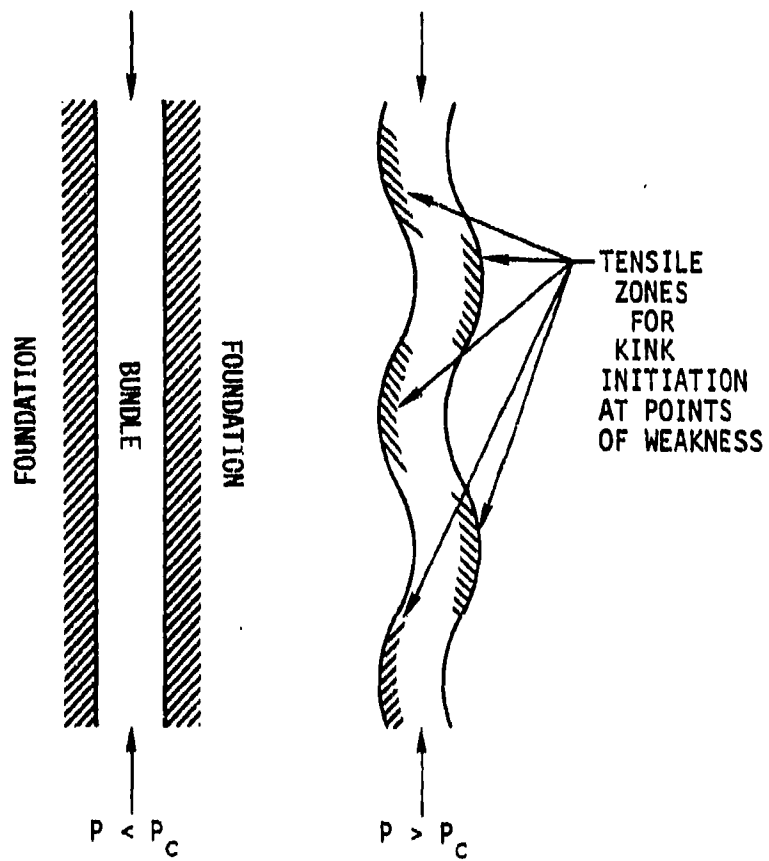
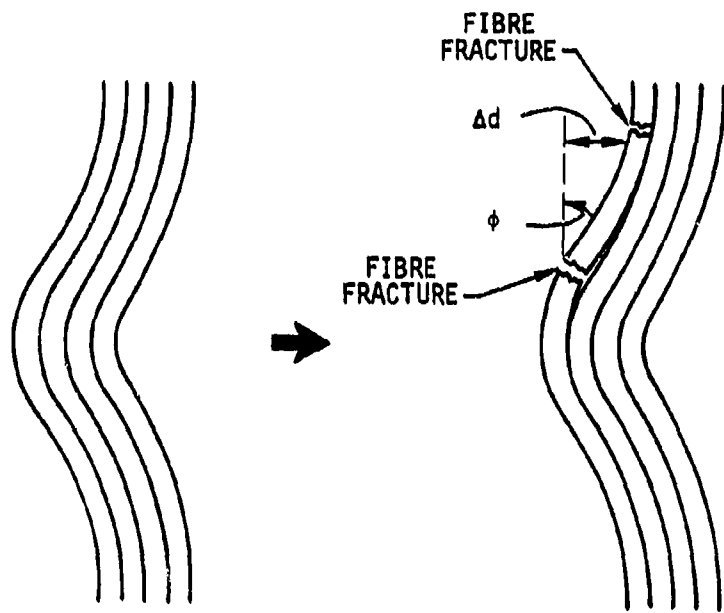
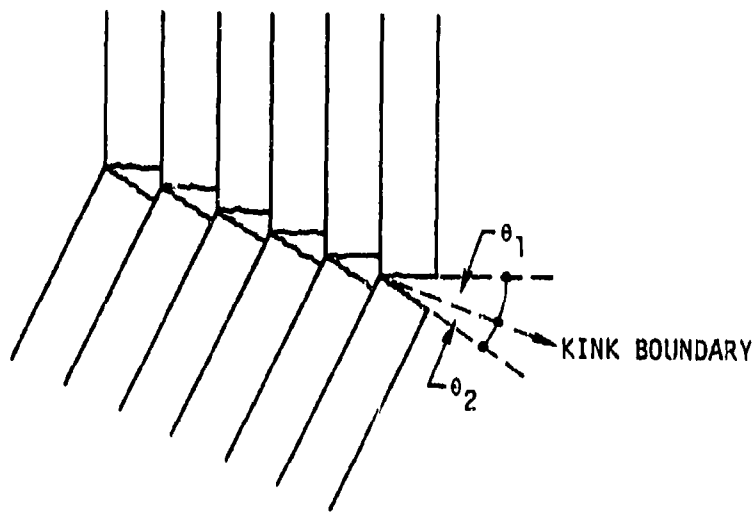


Fig. 40



a) BUCKLED CONFIGURATION

b) KINK INITIATION



c) KINK PROPAGATION

Fig. 41

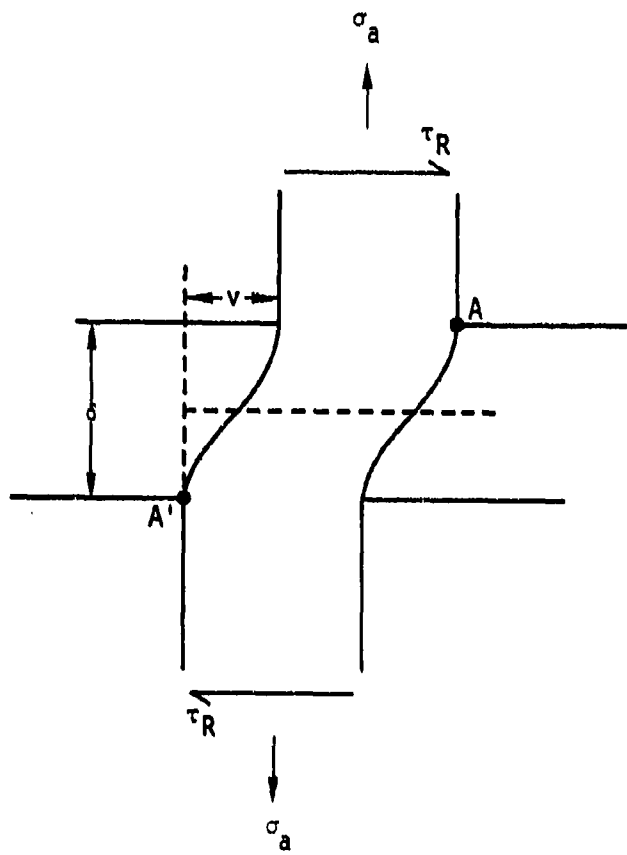


Fig. 42